Dynamics and Combined Frequency Voltage Control of Downhole Oil Pumping System

Weicheng Li[a,b], Vahid Vaziri[b], Sumeet S Aphale[b], Shimin Dong[a], Marian Wiercigroch[b,*]

[a] *School of Mechanical Engineering, Yanshan University, Qinhuangdao, 066004, China*
[b] *Centre for Applied Dynamics Research, School of Engineering, University of Aberdeen, Aberdeen AB24 3UE, UK*

Abstract

The motor load torque of a typical pumping system employed in onshore oil-fields has a fluctuating 'double-hump' profile, which requires a motor with a substantially higher rating than the average load torque. In this paper, we have developed a dynamical model of this electro-mechanical system. To reduce the load fluctuation and consequently lower the required motor rating and energy consumption, a real-time voltage and frequency optimization scheme (RTVFOS) is proposed. Both real-time frequency optimization scheme (RTFOS) applying constant voltage and frequency ratio principle as well as real-time voltage regulation scheme (RTVRS) with constant frequency are also simulated. It is shown that the RTFOS is capable of substantively decreasing the motor rating while the RTVRS is capable of delivering a significant energy savings. It is demonstrated that the RTVFOS combines the benefits of both control methods and also lowers the range of variation in voltage, thereby improving the motor's operating life.

Keywords: Dynamics; Frequency and voltage control; Energy saving; Pumping system; Electro-mechanical model.

1. Introduction

Sucker-rod pumping (SRP) systems are the most popular in onshore oil extraction and have an important market share in commercially viable oil-fields (see, e.g. [1–5]). Though a typical SRP system driven by constant voltage and frequency (CFV) power source has a stable operation, delivers reliable performance and has low manufacturing costs; it consumes a large amount of energy. There are nearly 570,000 SRP plants around the world and the average power of each device is about 10 kW (see, e.g. [6, 7]). If each plant could save just 10 %, a total of approximately 0.41×10^{10} kW-h could be saved in one year.

A SRP typical plant shown in Fig. 1 is comprised of a plunger, a rod string, a polished rod, a mechanical linkage including walking beam, pitman and crank, a gearbox, a belt transmission and an induction motor.

*Corresponding author.
Email address: m.wiercigroch@abdn.ac.uk (Marian Wiercigroch)

A motor drives a mechanical linkage via a belt transmission and gearbox, and the mechanical linkage converts the prime mover's rotary motion into the plunger's linear reciprocating movement, thereby this artificial lift plant pumps the oil during the upstroke and discharges it during the downstroke. The power consumed during each lift cycle can be attributed to four factors (see, e.g. [8]): (i) effective work during artificial lift, (ii) friction loss in the surface transmission parts, (iii) downhole transmission loss and (iv) motor inner losses. As the pumping parameters optimization methods have been adopted to maintain a good pumping operation and downhole efficiency (see, e.g. [7, 9–12]), there are efforts to reduce the motor inner losses (see, e.g. [13]).

As shown in Fig. 2, the motor load torque profile of a SRP system typically shows a 'double-hump' characteristics due to its usual operating regime (upstroke loading and downstroke unloading) and the contribution of a counter-weight mounted on a crank (see, e.g. [8, 14]). This high fluctuation of torque requires a motor with a substantially higher rating than the average load torque. To reduce the load torque variation, a number of engineering solutions including new designs of pumping systems (see, e.g. [15, 16]), modifying existing structure (see, e.g. [14]) and developing new motor types (see, e.g. [17, 18]) have been used. However, it is expensive to retrofit or swap a SRP system while in service and hence most of the above mentioned solutions are not popular. In recent years, variable frequency drives have been widely adopted to automatically adjust the strokes/min (SPM) pumping rate of a SRP system (see, e.g. [19–21]).

As altering a SPM affects the production, a dual pulse-width modulation frequency converter is proposed with the control strategy of adjusting the speed ratio between upstroke and downstroke, which saves the energy in one operating period (see, e.g. [22]). This is followed by a RTFOS utilizing the system's inertial load and keeping the SPM constant (see, e.g. [23]). Though this effectively reduces the rated motor requirements, it adopts the classical constant voltage per frequency (V/F) control principle, thereby limiting the potential energy savings.

For a general frequency converter, it takes the constant V/F control principle to maintain the motor's rated flux and keep motor output capacity unchanged (see, e.g. [24]). However, this control principle results in the energy waste if the load is below its rated value (see, e.g. [25]). Since the 1980s, different control methods have been proposed to employ different V/F ratios to adapt the demand of load and speed, thereby improving the motor efficiency and energy saving (see, e.g. [26–31]). As described above, the load of SRP presents a periodic fluctuation and the RTFOS, which can reduce the load fluctuation and energy waste. Based on this condition, the energy can be further saved if the voltage varies with the load to reduce the flux, instead of following the frequency to maintain the rated flux.

The paper is structured as follows. Section 2 presents an electro-mechanical model for SRP system

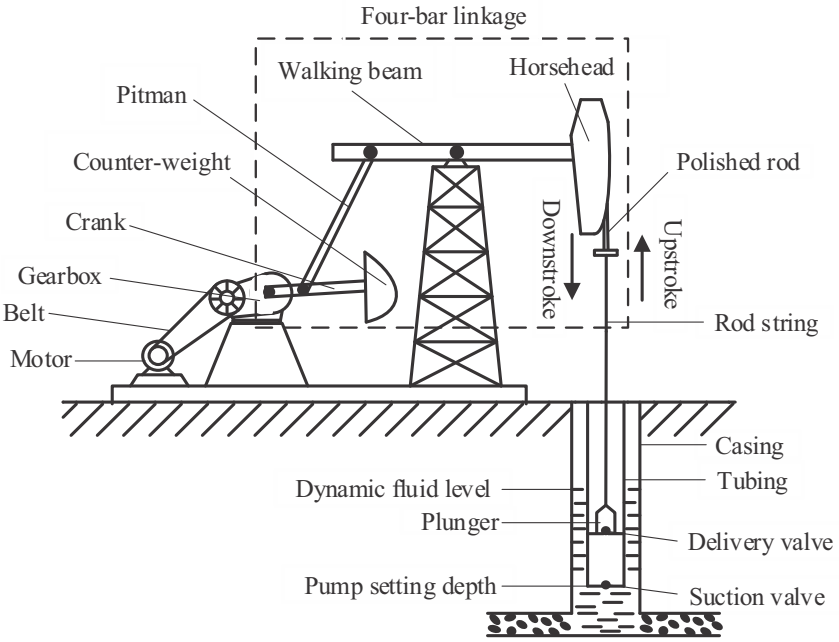

Figure 1: Sucker-rod pumping system. A motor provides power to drive a crank via a belt conveyor gear reducer, and this rotation motion is converted into a linear alternating motion of the rod string by a four-bar linkage. During the upstroke, the fluid contained in the tubing above the delivery valve is lifted to the surface, and the fluid is absorbed into the barrel while the suction valve opens. During the downstroke, the fluid is discharged out of the barrel while the delivery valve opens and the fluid weight is transferred from the plunger to the suction valve.

including the iron loss, which is valid under the condition of real time varying of frequency and voltage. Section 3 analyzes the SRP system transient and steady responses. Section 4 uses the field-recorded data of ground dynamometer card and motor input power for validating the proposed electro-mechanical model. Section 5 proposes a RTVFOS to reduce the load fluctuation and consequently to save energy. Section 6 gives comparisons of RTFOS, RTVRS and RTVFOS. In section 7 some conclusions and recommendations are drawn.

2. SRP system model

For a SRP system shown in Fig. 1, an electric motor provides the driving power (torque) to the mechanical system that generates an artificial lift. Thus, the SRP system model consists of an electric motor model and a model of the artificial lift delivering mechanical system.

2.1. Electric motor model

A typical induction motor is generally used as the actuator of choice for the SRP system (see, e.g. [13, 32]). The equivalent circuit of the motor represented in the *d-q* synchronously rotating frame that accounts for the iron loss, is employed to simulate the motor dynamic response (see, e.g. [13, 33]). This

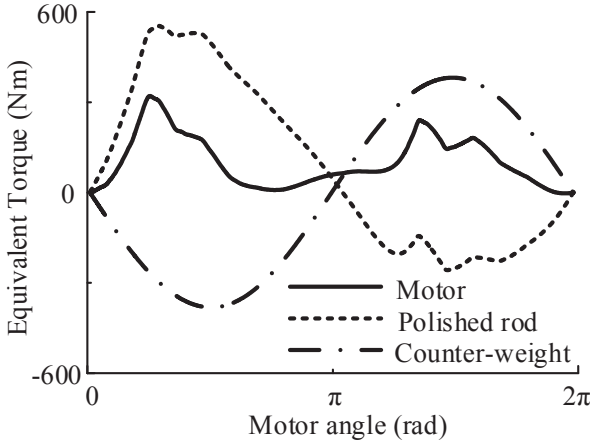

Figure 2: A typical motor load of the SRP system showing equivalent torques of motor, polished rod and counter-weight. The motor torque mainly resists the load from the polished rod and crank counter-weight at a constant speed. As the polished rod load is loaded during the upstroke and unloaded during the downstroke, an approximate sine wave torque is formed at the motor output shaft. Then the motor load presents a double-hump characteristics with the contribution of a crank counter-weight producing a cosine wave torque, for more details see, e.g. [8, 14, 15].

motor model is depicted in Fig. 3. Since the rotor flux in d-axis $\psi_{dr} = l_{lr}i_{dr} + l_m i_{dm}$ and the rotor flux in q-axis $\psi_{qr} = l_{lr}i_{qr} + l_m i_{qm}$, the voltage equations for these circuits are derived using Kirchhoff's Voltage Law.

$$
\begin{aligned}
&l_{lr}\frac{di_{dr}}{dt} + l_m\frac{di_{dm}}{dt} - (\omega_0 - \omega_r)\psi_{qr} + R_r i_{dr} = 0,\\
&l_{lr}\frac{di_{qr}}{dt} + l_m\frac{di_{qm}}{dt} + (\omega_0 - \omega_r)\psi_{dr} + R_r i_{qr} = 0,\\
&l_{ls}\frac{di_{ds}}{dt} + l_m\frac{di_{dm}}{dt} - \omega_0 l_{ls} i_{qs} - \omega_0 l_m i_{qm} + R_s i_{ds} = U_{ds},\\
&l_{ls}\frac{di_{qs}}{dt} + l_m\frac{di_{qm}}{dt} + \omega_0 l_{ls} i_{ds} + \omega_0 l_m i_{dm} + R_s i_{qs} = U_{qs},\\
&l_m\frac{di_{dm}}{dt} - \omega_0 l_m i_{qm} - R_{Fe}(i_{ds} + i_{dr} - i_{dm}) = 0,\\
&l_m\frac{di_{qm}}{dt} + \omega_0 l_m i_{dm} - R_{Fe}(i_{qs} + i_{qr} - i_{qm}) = 0,
\end{aligned}
\tag{1}
$$

where

$$
\begin{aligned}
U_{ds} &= (\frac{\sqrt{6}}{3}U_a - \frac{\sqrt{6}}{6}U_b - \frac{\sqrt{6}}{6}U_c)\cos\theta_s + (\frac{\sqrt{2}}{2}U_b - \frac{\sqrt{2}}{2}U_c)\sin\theta_s,\\
U_{qs} &= -(\frac{\sqrt{6}}{3}U_a - \frac{\sqrt{6}}{6}U_b - \frac{\sqrt{6}}{6}U_c)\sin\theta_s + (\frac{\sqrt{2}}{2}U_b - \frac{\sqrt{2}}{2}U_c)\cos\theta_s,\\
\omega_0 &= 2\pi f, \quad \omega_r = n_p\theta'_m.
\end{aligned}
\tag{2}
$$

Here, $\theta_s = \int_0^t \omega_0 dt$ is the rotating angle of the d-q coordinate system; ω_0 is the synchronous velocity of the electric angle of motor; f is the motor driving frequency; ω_r is the velocity of electric angle of motor; n_p is the number of motor pole-pairs; θ_m is the mechanical angle of motor; i_{ds}, i_{qs} are the stator currents in d-axis and q-axis respectively; i_{dm}, i_{qm} are the field currents in d-axis and q-axis respectively; i_{dr},

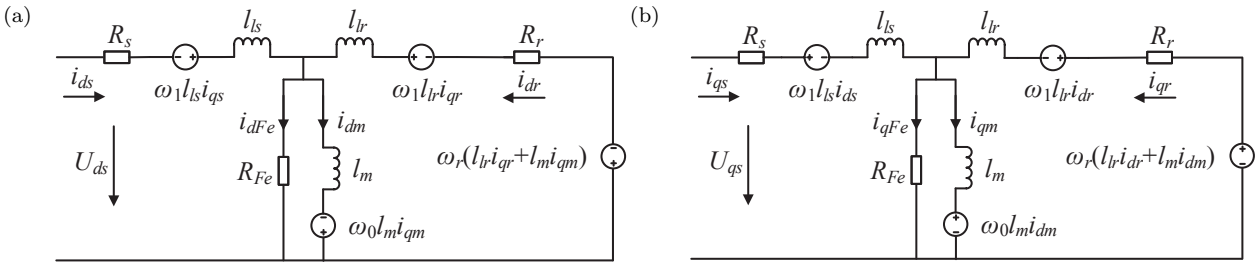

Figure 3: Equivalent circuits of an induction motor including the iron loss in the synchronously rotating frame: (a) d-axis and (b) q-axis.

i_{qr} are the rotator currents in d-axis and q-axis respectively; R_s, R_r, R_{Fe} are the resistances of stator, rotor and iron core respectively; l_{ls}, l_{lr}, l_m are the stator leakage inductance, rotator leakage inductance and mutual inductance respectively.

In this paper, as the controlled driving frequency and voltage vary in real-time with the load, the universal expression of three-phase voltage U_i $(i = a, b, c)$ given in Eq. (3) is replaced with that given in Eq. (4).

$$U_i = 220\sqrt{2}\sin(2\pi f t + \varphi_i), \tag{3}$$

$$U_i = U_m\sqrt{2}\sin(2\pi \int_0^t f dt + \varphi_i), \tag{4}$$

where $\varphi_i = 0, -\frac{2}{3}\pi, -\frac{4}{3}\pi$ while $i = a, b, c$, respectively and U_m is the effective value of the voltage.

The motor driving torque, M_m, can be represented in the state-variables of Eq. (B.1).

$$M_m = \frac{n_p l_m}{l_m + l_{lr}}\left[\psi_{dr}(i_{qm} - \frac{\psi_{qr}}{l_{lr}} + \frac{l_m i_{qm}}{l_{lr}}) - \psi_{qr}(i_{dm} - \frac{\psi_{dr}}{l_{lr}} + \frac{l_m i_{dm}}{l_{lr}})\right]. \tag{5}$$

2.2. Mechanical system model

The mechanical part of a SRP system shown in Fig. 1 combines two interacting systems viz: (i) A surface transmission system and (ii) A downhole pumping system. Prior to establishing the mechanical system model, some simplifying assumptions are made as follows: (i) By neglecting torsional and bending deformations, the surface transmission system is simplified as a single-degree-of-freedom system (see, e.g. [8, 13, 32, 34, 35]), (ii) The tubing string is presumed to be vertical and anchored at the pump setting depth, (iii) Only the longitudinal vibration of rod string is considered (see, e.g. [13, 32, 34]) and (iv) The initial position of the polished rod is at the bottom of stroke.

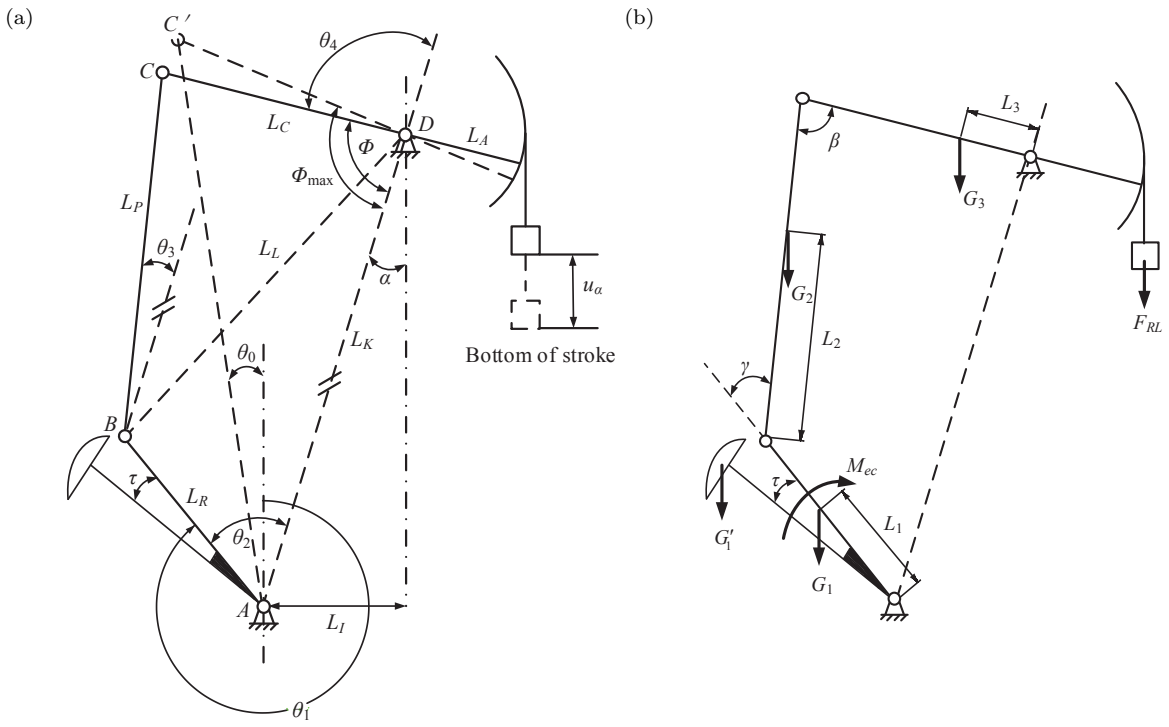

Figure 4: Schematic diagrams of the four-bar linkage. (a) Motion sketch. The crank drives the polished rod moving from the bottom of stroke. (b) Force sketch. The equivalent resistive torque of the crank is used for balancing the torque from the polished rod rod and the gravity of each component.

2.2.1. Surface transmission model

To model the surface transmission system, a single-degree-of-freedom system is used. Its equation of motion is established by the work energy theorem and can be expressed as:

$$d(\frac{1}{2}J_e(\theta'_m)^2) = (M_m - M_{eq})\theta'_m dt, \tag{6}$$

and

$$J_e = \sum J_i(\frac{\omega_i}{\theta'_m})^2 + \sum m_i(\frac{v_i}{\theta'_m})^2, \tag{7}$$

$$M_{eq} = \frac{M_{ec}}{\varepsilon_{mc}\eta_{mc}\eta_{cp}}, \tag{8}$$

where J_e is the equivalent moment of inertia of the surface transmission system; J_i, m_i, ω_i and v_i are the moment of inertia, mass, angular velocity and velocity of the centre of mass of each component in this surface transmission system; M_{eq} is the equivalent resistive torque of the motor; M_{ec} is the equivalent resistive torque of the crank; η_{mc} is the transmission efficiency from the motor to the crank; η_{cp} is the transmission efficiency from the crank to the polished rod; ε_{mc} is the transmission ratio from the motor

to the crank.

As a part of the equivalent moment of inertia, decided by the four-bar linkage, varies with time; Eq. 6 can be rewritten as:

$$J_e\theta''_m + \frac{1}{2}\theta'_m J'_e = M_m - M_{eq} = M_m - \frac{M_{ec}}{\varepsilon_{mc}\eta_{mc}\eta_{cp}}, \tag{9}$$

A schematic diagram of the four-bar linkage geometry is shown in Fig. 4. Eq. (10) represents the equivalent resistive torque of the crank is derived based on this geometry, a full derivation of which is included in Appendix A.

$$\begin{aligned} M_{ec} = &\left[-\frac{\sin(\theta_2-\theta_3)}{L_C\sin(\theta_4-\theta_3)}(F_{RL}L_A - G_3L_3\sin(\theta_4-\alpha)) - G_2\sin\theta_1\right]L_R \\ &+ G_1L_1\sin(\theta_2-\alpha) + G'_1L_R\sin(\theta_2-\alpha+\tau), \end{aligned} \tag{10}$$

where F_{RL} is the polished rod load; G_1, G_2, G_3 and G'_1 are the weights of the crank, the pitman, the walking beam and the counter-weight respectively and τ is the offset angle of the counter-weight.

As depicted in Fig. 4a, the position of the polished rod derived as:

$$\begin{aligned} u_a =&(\phi_{max}-\phi)L_A, \\ =&\left[\arccos(\frac{L_K^2+L_C^2-(L_R+L_P)^2}{2L_KL_C}) - \arccos(\frac{L_L^2+L_C^2-L_P^2}{2L_CL_L}) - \arcsin(\frac{L_R}{L_L}\sin\theta_2)\right]L_A, \\ =&\Bigg[\arccos(\frac{L_K^2+L_C^2-(L_R+L_P)^2}{2L_KL_C}) - \arccos(\frac{L_L^2+L_C^2-L_P^2}{2L_CL_L}) \\ &- \arcsin(\frac{L_R}{L_L}\sin(2\pi-\frac{\theta_m}{\varepsilon_{mc}}+\theta_0+\alpha))\Bigg]L_A. \end{aligned} \tag{11}$$

2.2.2. Downhole pumping model

The rod string transmits the reciprocating motion of polished rod to the plunger and consequently, the oil can be pumped (lifted) and discharged in one period. As the rod string is typically several kilometers long, it mainly produces a significant longitudinal vibration during this reciprocating motion. As a result, the one-dimensional wave equation is generally used to describe this process (see, e.g. [7, 34, 36, 37]). In this paper, the rod string is assumed to be an elastic component that is exposed to excitations from the polished rod motion and the pump load; its arbitrary micro element suffers the inertial load, the damping force, the axial force and gravity. A physical model of rod string's longitudinal vibration accounting for all the aforementioned loads is shown in Fig. 5. Based on this, the rod string wave equation with two boundary conditions can be expressed as:

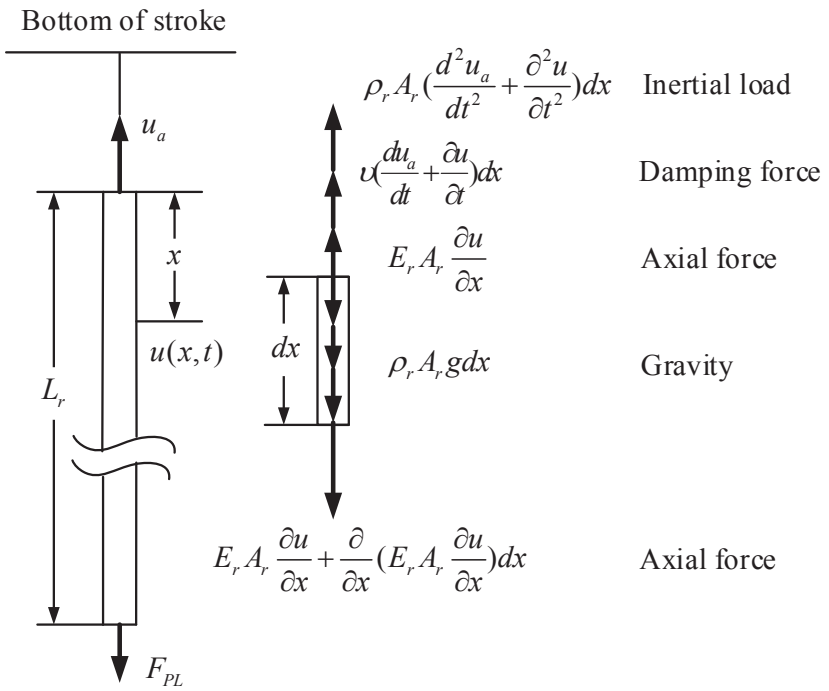

Figure 5: Physical model of the rod string of the downhole transmission system. The rod string is treated as an elastic element that exposed to excitations from the polished rod motion and the pump load, generating longitudinal vibration.

$$\begin{aligned} \frac{\partial^2 u(x,t)}{\partial t^2}-\frac{E_r}{\rho_r}\frac{\partial^2 u(x,t)}{\partial x^2}+\frac{\upsilon}{\rho_r A_r}\frac{\partial u(x,t)}{\partial t} &= -\frac{d^2 u_a}{dt^2}-\frac{\upsilon}{\rho_r A_r}\frac{du_a}{dt}, \\ u(x,t)\mid_{x=0} &= u_a, \\ E_r A_r \frac{\partial u(x,t)}{\partial x}\mid_{x=L_r} &= F_{PL}, \end{aligned} \tag{12}$$

where $u(x,t)$ is the displacement of the rod string at an arbitrary depth and time; F_{PL} is the pump load described; υ is the liquid-to-rod string damping coefficient (see, e.g. [35]); L_r, E_r, A_r, ρ_r are the length, elastic modulus, cross-section area and density of rod string respectively.

As the rod string's longitudinal vibrations are not dependent on its self-weight, the gravity term is omitted from the wave equation and its effect is incorporated while calculating the polished rod load as expressed in Appendix B.

The pump load generated by the pressures acting on the upper and lower surfaces of the plunger are expressed in Eq. (13). The pump outlet pressure, p_d, is produced by the tubing head pressure and the liquid column in the tubing, and can be calculated from Eq. (14).

$$F_{PL} = A_p(p_d - p) - A_r p_d, \tag{13}$$

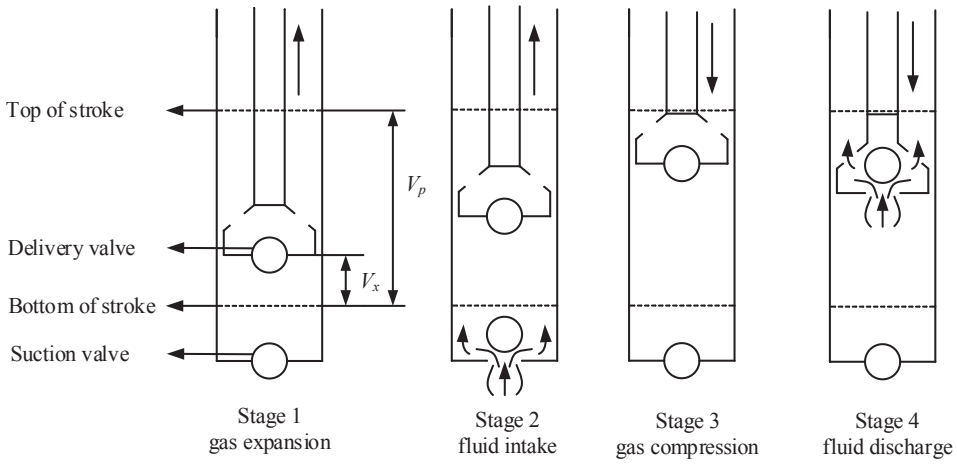

Figure 6: The four stages for one pumping oil period from pumping to discharging. The plunger moves up from the bottom of stroke and the pump pressure decreases, and the fluid is absorbed into the barrel while the suction valve is open; As the plunger arrives at the top of stroke, it moves down and the pump pressure rises, and the fluid is drained out of the barrel while the delivery valve is open.

$$p_d = p_t + ((1 - \eta_w)\rho_o + \rho_w \eta_w) g L_p, \tag{14}$$

where A_p is the cross-section area of the plunger, p_d is the pump outlet pressure, p is the pressure in the pump cylinder, p_t is the tubing head pressure, η_w is the water content, ρ_o is the oil density, ρ_w is the density of water, g is the gravitational acceleration and L_p is the pump setting depth.

The pump operating principle is schematically shown in Fig. 6. Its operation can be divided into four stages viz:

- Stage 1. Prior to the opening of the suction valve, the plunger moves up from the bottom of stroke and the pump pressure decreases.
- Stage 2. When the pump pressure reduces to pump inlet pressure, the suction valve is open and the fluid is absorbed into the barrel.
- Stage 3. As the plunger arrives at the top of stroke, the suction valve is closed and the pump pressure rises while the plunger begins its downstroke.
- Stage 4. Finally, as the pump pressure increases to pump outlet pressure, the delivery valve is open and the fluid is drained out of the barrel.

Some assumptions made while creating the pump mathematical model are: (i) No movement of the valve ball, (ii) Incompressible liquid, (iii) No phase change from gas to liquid and (iv) No pressure drop

while fluid is passing through a valve. Hence, the pressure, p, can be expressed as:

$$p = \begin{cases} (\dfrac{V_{og}}{V_{og}+V_x})^n p_d, & \text{Stage 1 : if } v_p > 0 \quad \text{and} \quad p > p_s \\ p_s, & \text{Stage 2 : if } v_p > 0 \quad \text{and} \quad p = p_s \\ (\dfrac{V_g}{V_g-(V_p-V_x)})^n p_s, & \text{Stage 3 : if } v_p < 0 \quad \text{and} \quad p < p_d \\ p_d, & \text{Stage 4 : if } v_p < 0 \quad \text{and} \quad p = p_d \end{cases} \tag{15}$$

where V_{og} and V_g are the gas volume in the pump when plunger arrives at the bottom and top of the stroke respectively, V_p is the pump stroke volume, V_x is the pump displacement volume, n is the gas polytropic exponent, p_s is the pump intake pressure produced by the casing head pressure and the liquid column in the casing and v_p is the velocity of the plunger.

2.3. Numerical simulation of the entire SRP model

A complete SRP mathematical model consisting of seventeen first-order differential equations has been developed and is shown in Appendix B. The model comprising seventeen state variables, namely, $\boldsymbol{X} = [\psi_{dr}, \psi_{qr}, i_{ds}, i_{qs}, i_{dm}, i_{qm}, \theta_m, \omega_m, x_{11}, x_{12}, x_{21}, x_{22}, x_{31}, x_{32}, x_{41}, x_{42}, p]$, is solved numerically using the Runge-Kutta method with an automatic integration step control. As the system numerical model contains multi-variables and has strong coupling, the MATLAB having abaundant solver package is employed to solve the equations in this paper. Differential equations describing this dynamical system are stiff. A trial and error method is adopted to seek the desired solution for the given set of equations. Consequently, the ode15s with a relative tolerance of 0.00001 is used to ensure convergence to the desired solution. System steady state responses are obtained in less than 1 s, which is computationally acceptable. A flow chart sequencing all the operations that need to be carried out to simulate the model for one period, T, is given in Appendix B. The five main steps in this sequence are:

(i) With the system parameters and initialized state variables, the state variables, $\psi_{dr}, \psi_{qr}, i_{ds}, i_{qs}, i_{dm}$, i_{qm}, are updated using state equations for the motor given in Eq. (B.1), thereby generating a motor driving torque. The initial system loads are also obtained.

(ii) Since the driving torque and equivalent resistive torque are obtained, the state variables, θ_m and ω_m, are updated by Eq. (B.2) and then the motion of the polished rod is computed using Eq. (11).

(iii) The rod string wave equation can be solved while the excitations from the motion of the polished rod and pump load are confirmed, and the state variables, $x_{11}, x_{12}, x_{21}, x_{22}, x_{31}, x_{32}, x_{41}, x_{42}$, in Eq. (B.14) are updated. Consequently, the motion of plunger can be computed using Eqs (B.17) and (B.18).

(iv) The motion of the plunger decides the pump pressure, p, and this state variable is updated using Eq. (B.16), depending on the velocity direction of plunger and its current value.

(v) The state variables are updated completely for one step. The simulation is completed if one of the following conditions is met: (i) the time exceeds one operating period of the SRP system, (ii) the motor driving torque or the polished rod load exceeds its allowable maximum value.

3. Dynamic responses of system

The basic parameters and motor parameters of one test well from Changqing Oilfield are listed in Tables 1 and 2, respectively. Since our purpose is studying the periodic operation of SRP system, the initial motor speed is set by its nominal value. Combining with the assumption that the initial position of the polished rod is at the bottom of stroke, the initial motor angle, θ_{m0}, can be confirmed with Eq. (A.5) and transmission ratio between motor and crank, and the initial pump pressure equals the pump outlet pressure, p_d, depicted in the pump operating mechanism. The initial values of other state variables are all confirmed with hitting to zero. Therefore, the initial values of all the state variables are given as

$$\boldsymbol{X} = [0, 0, 0, 0, 0, 0, 0, \theta_{m0}, \omega_n, 0, 0, 0, 0, 0, 0, 0, 0, p_d], \tag{16}$$

where ω_n is the rated value of angular velocity of motor.

With the above initial conditions and well parameters, Figs 7 and 8 present the simulation results of the main transient and steady-state responses of the SRP system driven by a CFV power source. Note that the SRP system starts when the polished rod moves up from the bottom of stroke. The transient state responses depicted in Fig. 7 can be analyzed as follows:

(i) The pump pressure is at its maximum pressure equalling to the pump outlet pressure at the beginning. As the rod string is more than one kilometer long, a sudden excitation makes the pump pressure produce a vibration while the polished rod begins to move up and the pump pressure decreases with the increasing gas volume.

(ii) As shown in Eq. (13), the pump load is decided by the pump pressure. Therefore, it starts at its minimum and increases with the polished rod moving up, in tandem with the generated vibration.

(iii) The polished rod load is composed of pump load, rod string weight, inertial load, vibration load and friction load. Therefore, it starts with a positive value, having little vibration. The load and the weight of walking beam and pitman produce a polished rod torque acting on the crank via the four-bar linkage. This torque is the first term in Eq. (10). The initial polished rod torque is only provided by

the weight of the walking beam, G_2, with the initial condition $\theta_2 = \theta_3$. This increases with time during this loading process. The counter-weight torque is the sum of the last two terms in Eq. (10) and is employed for balancing the polished rod torque. Therefore, it begins to decrease from the initial value. The equivalent resistive torque of the crank is the sum of these two load torques.

(iv) The motor torque, equivalent inertial torque, motor speed as well as rotor and stator currents in the d-q synchronously rotating frame all have an oscillation in the beginning and need 0.1 s to converge. This is because its nominal speed is set as the initial value of motor speed, without matching initial value for the state variables in the motor model.

It can be seen that the SRP system takes 0.1 s to settle in steady state, and the steady state responses depicted in Fig. 8 can be analyzed as follows:

(i) The pump pressure presents a variation matching with the pump operating mechanism as described in Subsection 2.2.2.

(ii) As the pump load is decided by the pump pressure variation shown in Eq. (13), it follows an inverse trend to that of the pump pressure.

(iii) The polished rod load is composed of pump load, rod string weight, inertial load, vibration load and friction load. This load and the weight of walking beam and pitman generate a sinusoidal torque acting on the crank via the four-bar linkage.

(iv) As the counter-weight and the weight of crank bring a torque with a cosine trend, the crank static torque presents a double-hump characteristics due to the combination of the polished rod load, the counter-weight and the weight of four-bar linkage.

(v) The belt conveyor gear reducer is a rigid body capable of amplifying torque and reducing speed. The motor torque is generated by the equivalent resistive torque of the crank and equivalent inertial torque (left-hand term in Eq. (9)). As the SRP system is driven by a constant power frequency, the equivalent inertial torque is small and the motor torque have a trend similar to the crank torque. The motor speed undergoes a subtle change against the motor torque.

(vi) The rotor and stator current in the d-q synchronously rotating frame vary with the motor load.

4. Model Validation

For a SRP system, the ground dynamometer card (records a polished rod displacement and a polished rod load in one SRP's period) and the motor input power curve in one SRP's period are generally used to verify the accuracy of a SRP system simulation model (see, e.g. [1, 4, 8, 35, 37, 38]). In this paper, the field data are obtained though the Supervisory Control And Data Acquisition (SCADA) system, and the

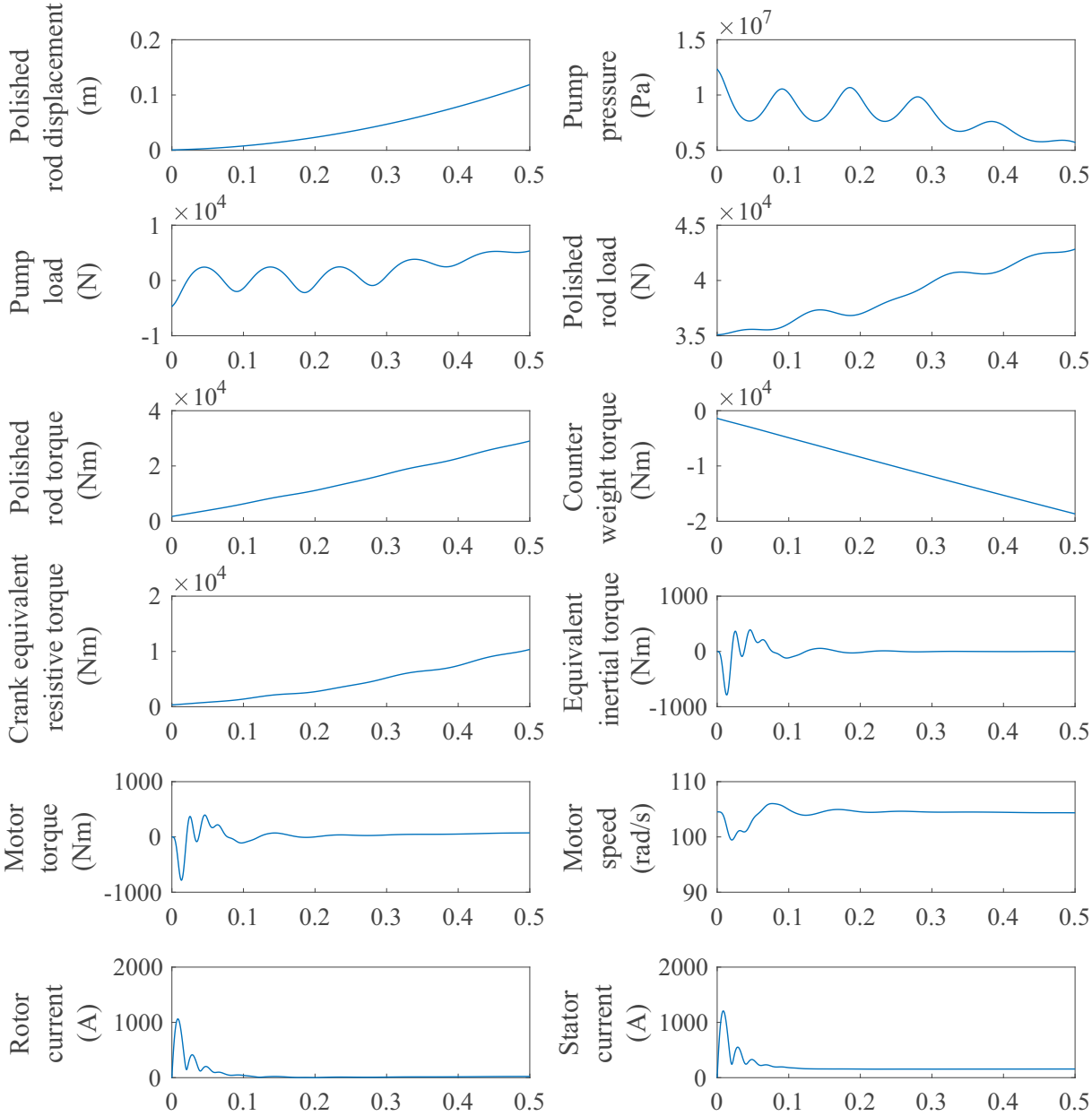

Figure 7: Transient state responses of SRP system. These transient state responses in 0.5 s is clearly plotted with the given initial value of state variables in Eq. (16). Since the initial values of the state variables in the motor model are not matching with the initial motor speed (nominal value), the current, torque and speed have an oscillation and needs 0.1 s to converge.

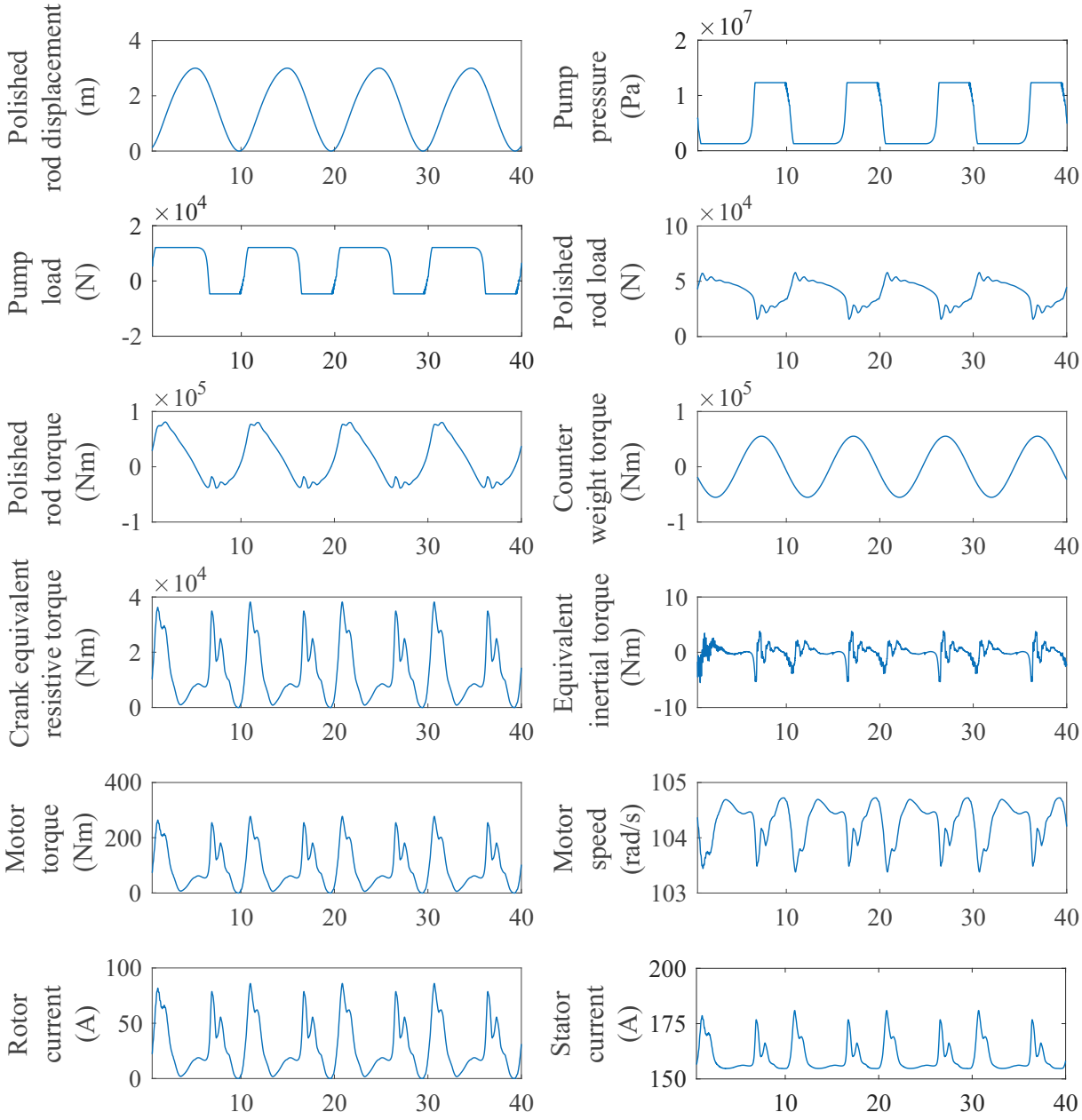

Figure 8: Steady state responses of SRP system. Its starting time is 0.5 s in order to eliminate the effect of oscillation in transient state responses and have a clear view for the steady state responses. It can be seen that all these dynamic responses present a periodic variation with the reciprocating movement of polished rod.

Table 1: Oil well basic parameters

Well number	X49-32	**SRP type**	CYJ10-3-53HB
Motor type	Y250M-6	**Stroke length**	3 m
SPM	6 min^{-1}	**Pump diameter**	44 mm
Pump setting depth	1200 m	**Rod string diameter**	22 mm
Rod string length	1200 m	**Counter-weight**	41.16 kN
Reservoir midpoint	1500 m	**Oil density**	850 kg/m^3
Water content	97.4 %	**Dynamic liquid level**	1100 m
Casing head pressure	0.3 MPa	**Tubing head pressure**	0.6 MPa
Fluid viscosity	0.086 Pa·s	**Gas oil ratio**	60 m^3/m^3

Table 2: Motor parameters

Rated power	37 kW	**Rated speed**	980 rpm
Rotor rotary inertia	0.834 kg·m^2	**polar pairs**	3
Stator resistance	0.082 Ω	**Rotor resistance**	0.050 Ω
iron loss resistance	60 Ω	**Rotor self-inductance**	0.02783 H
Stator self-inductance	0.02783 H	**Mutual inductance**	0.02711 H

primary processes of data acquisition, transmission, processing and displaying are described as follows, (i) the load sensor is mounted on the polished rod and the angular displacement sensor is mounted on the bearing support of the walking beam to detect the ground dynamometer card, (ii) the electrical measuring instrument is mounted in the control cabinet to detect the motor input power, (iii) these field data are transmitted to the SQL Server database by the remote data terminal, and are saved in hexadecimal notation and (iv) the ground dynamometer card and motor input power are displayed on the computer after converting the original data into decimal data.

Fig. 9 depicts the comparison curve of ground dynamometer card and motor input power between the simulation and test results. The maximum and minimum polished rod load of the simulation results are 58.71 kN and 16.96 kN, with relative errors of 4.33 % and 5.80 % respectively compared to the corresponding results of field tests (61.37 kN and 16.03 kN). The maximum and minimum motor input power of the simulation results are 32.61 kW and 2.30 kW, with relative errors of 6.35 % and 6.12 % respectively compared to the corresponding results of field test (34.82 kW, 2.45 kW). Therefore, the SRP system simulation model proposed in this paper agrees well with the field experiments and will be employed for further analysis.

5. Voltage and frequency optimization control scheme

The RTVFOS proposed in this paper consists of two parts namely: (i) A real-time frequency optimization aimed at redistributing the system inertial load, to reduce the load variation, motor copper

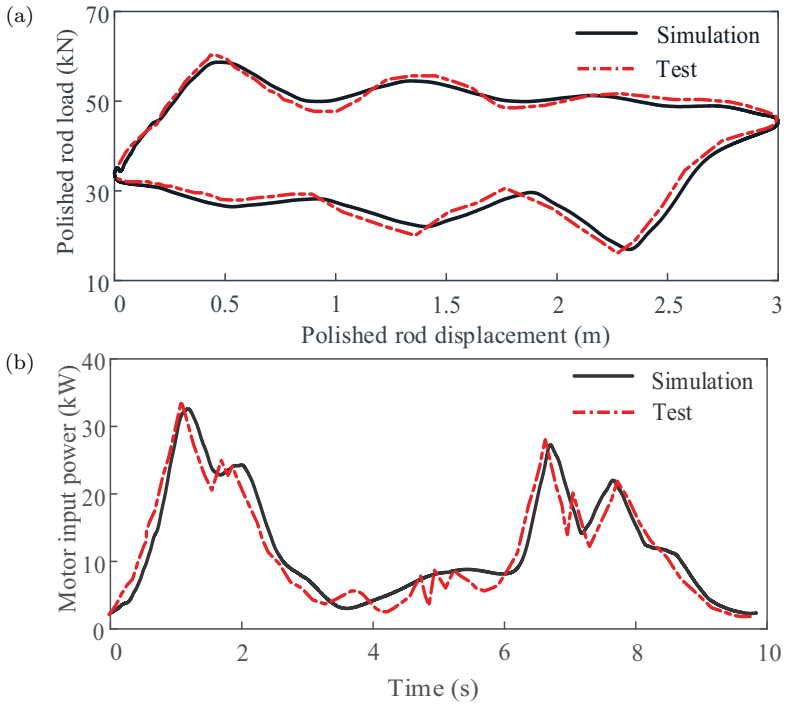

Figure 9: SRP system simulation model precision verification by collecting the field data of the oil well listed in Table I. (a) Ground dynamometer card. (b) Motor input power.

loss and motor rating and (ii) A real-time voltage regulation based on the optimized frequency, aimed at saving energy by reducing magnetic flux.

5.1. Real-time frequency optimization scheme

As described in the preceding paragraph, a reduction in load fluctuations allows reducing the overall motor rating. This consequently reduces motor copper loss and results in significant energy savings. The inertial load depending on the velocity distribution for this multi-component system is a vital share of the total load (see, e.g. [17]). The frequency optimization scheme is proposed to tweak the real-time motor speed to match the load variation, thereby reducing the fluctuation in one lift cycle.

5.1.1. Design variables

When the SRP system is in steady state and the SPM is confirmed, it has a constant period. Therefore, the power frequency controlling the motor speed in one period can be expressed in a Fourier series given by:

$$f(t) = a_0 + \sum_{j=1}^{N} [a_j \cos(j\frac{2\pi}{T}t) + b_j \sin(j\frac{2\pi}{T}t)], \tag{17}$$

where a_0 and (a_j, b_j) are the Fourier coefficients and T is the operating period of SRP system.

As the power frequency is decided by the Fourier coefficients, the Fourier coefficients are taken as the design variables to obtain an optimum power frequency for adapting the load:

$$x = \{a_0, a_1, b_1, \ldots, a_N, b_N\}. \tag{18}$$

5.1.2. Cost function

The instantaneous motor output power is a good indication of load fluctuations and motor efficiency. It also determines the rating-based motor selection. Therefore, the standard deviation, P_{std}, for one lift cycle is chosen as the optimization target. The corresponding cost function is then given by:

$$P_{std}(x) = \sqrt{\frac{1}{N}\sum_{i=1}^{N}(M_{mi}(x)\theta'_{mi}(x) - \overline{P(x)})^2} \quad \longrightarrow \quad minimum, \tag{19}$$

where $M_{mi}(x)$ and $\theta_{mi}(x)$ are the driving torque and mechanical angle of motor with the optimized Fourier coefficients of power frequency, respectively, $\overline{P(x)}=\frac{1}{N}\sum_{i=1}^{N}(M_{mi}(x)\theta'_{mi}(x))$ is the average value of motor output power and N is the number of discrete points in one lift cycle.

5.1.3. Constraint conditions

To maintain a constant SPM, the average motor speed of one cycle must be kept fixed - before and after applying the real-time frequency optimization. The SRP system is generally driven by a conventional induction motor whose speed is mainly decided by the power frequency and the number of poles. As the number of poles is fixed for a given machine, the above constraint on the SPM can be achieved if the average power frequency of one cycle at a constant frequency mode, $\bar{f}_c$, is equal to the one seen during the real-time frequency optimization mode, namely $\bar{f}_c = \bar{f}_o$.

Note that the periodic functions $\cos(j\frac{2\pi}{T}t)$ and $\sin(j\frac{2\pi}{T}t)$ given in Eq. (17) satisfy the following conditions:

$$\int_0^T \cos(j\frac{2\pi}{T}t)dt = 0, \quad \int_0^T \sin(j\frac{2\pi}{T}t)dt = 0. \tag{20}$$

Thus, the average power frequency resulting from the real-time frequency optimization is:

$$\bar{f}_o = \frac{\int_0^T f(t)dt}{T} = a_0. \tag{21}$$

In general, the supply power frequency is 50 Hz ($\bar{f}_c = 50$) while the SRP system is operating at a constant frequency. As the average power frequency after applying real-time frequency optimization $\bar{f}_o$ equals a_0 shown in Eq. (21), a_0 should be maintained at 50 so that the constant SPM is satisfied

before and after applying real-time frequency optimization. At the same time, the instantaneous power frequency should also have a suitable practical limit, besides, the polished rod load and motor torque shouldn't exceed their allowable value. Therefore, the conditions are as follows:

$$\begin{aligned} &a_0 = 50, \\ &f_d \leq f \leq f_u, \\ &F_{RL} \leq [F_{RL}], \\ &M_m \leq [M_m]. \end{aligned} \tag{22}$$

where f_u and f_d are the upper boundary and lower boundary of frequency, respectively; $[F_{RL}]$ is the allowable maximum of polished rod load (see, e.g. [13]); $[M_m]$ is the allowable maximum of motor torque, and it is generally 2∼2.2 times the nominal torque for the Y-series motor (see, e.g. [39]).

5.1.4. Optimization algorithm

The frequency optimization model is written as:

$$\begin{aligned} &\Omega(x) = \min\{P_{std}(a_0, a_1, b_1, \ldots, a_N, b_N)\}, \\ &f_d \leq f \leq f_u. \\ &F_{RL} \leq [F_{RL}], \\ &M_m \leq [M_m]. \end{aligned} \tag{23}$$

where $a_0 = 50$ is the fundamental frequency used for maintaining the SPM and $[a_1, b_1, \ldots, a_N, b_N]$ are the Fourier coefficients deciding the style of frequency in one period.

A genetic algorithm is applied to seek the Fourier coefficients that minimize P_{std}, mainly due to its search efficiency and robustness. MATLAB has a package of genetic algorithms called "ga" with the optional inputting parameters ('PopulationSize', 'Generations', 'EliteCount'), which is employed during this optimization process. Each of the above parameters is set to 100, 200, 10, respectively so as to balance the computing time and the accuracy of the optimized problem. A flow-chart for the employed frequency optimization scheme is shown in Fig. 10.

5.2. Real-time voltage regulation scheme

As the aim of this work is saving energy during steady-state operation of the SRP system, the steady-state equivalent circuit of the induction motor has been adopted. Furthermore, the leakage inductances

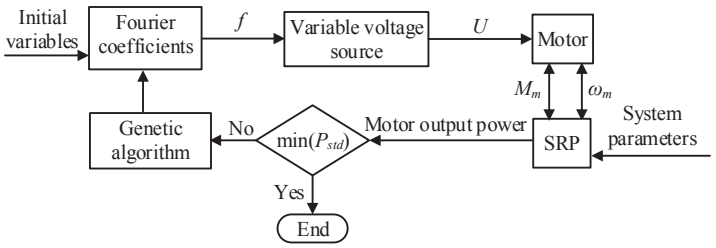

Figure 10: Flow-chart for the real-time frequency optimization - It uses system parameters as inputs and employs a genetic algorithm to generate optimized Fourier coefficients used for expressing the supply frequency that minimizes the P_{std}.

of stator and rotor are very small compared to the mutual inductance, and are neglected to simplify the model (see, e.g. [26]). Thus, the rotor and stator fluxes are simplified as:

$$\psi_{ds} = \psi_{dr} = l_m i_{dm}, \quad \psi_{qs} = \psi_{qr} = l_m i_{qm}. \tag{24}$$

With the above simplifications, the circuit shown in Fig. 3 can be reorginized to the one shown in Fig. 11, to represent the steady-state equivalent circuit of the system. The motor inner loss, P_{is}, mainly consists of stator copper loss, P_{Cus}, rotor copper loss, P_{Cur} and iron loss, P_{Fe}. Therefore,

$$P_{is} = P_{Cus} + P_{Cur} + P_{Fe}, \tag{25}$$

where

$$P_{Cus} = R_s(i_{ds}^2 + i_{qs}^2), \quad P_{Cur} = R_r(i_{dr}^2 + i_{qr}^2), \quad P_{Fe} = R_{Fe}(i_{dFe}^2 + i_{qFe}^2). \tag{26}$$

Variations in steady-state current are small enough (compared to the transients) and steady-state current is considered constant. Therefore, there is no voltage drop across the inductor in the steady-state equivalent circuit. In order to simplify the equation for motor inner loss, the steady-state equivalent circuit given in Fig. 11 is defined in the direction of the rotor flux (ψ_{ds}=ψ_{dr}=ψ_r, ψ_{qs}=ψ_{qr}=0) (see, e.g. [40]). Therefore, the currents depicted in Fig. 11 can be expressed as follows:

$$\begin{aligned}
&i_{dFe} = \frac{\omega_0 \psi_{qs}}{R_{Fe}} = 0, \quad i_{qFe} = \frac{\omega_0}{R_{Fe}} \psi_{ds} = \frac{\omega_0}{R_{Fe}} \psi_r, \quad i_{dr} = \frac{\omega_0 \psi_{qs} - \omega_r \psi_{qr}}{R_r} = 0, \\
&i_{qr} = \frac{\omega_r \psi_{dr} - \omega_0 \psi_{ds}}{R_r} = -\frac{\omega_s}{R_r} \psi_r, \quad i_{dm} = \frac{\psi_{ds}}{l_m} = \frac{\psi_r}{l_m}, \quad i_{qm} = \frac{\psi_{qs}}{l_m} = 0, \\
&i_{ds} = i_{dFe} + i_{dm} - i_{dr} = i_{dm} = \frac{\psi_r}{l_m},
\end{aligned} \tag{27}$$

where ψ_r is the flux in the field-oriented frame and $\omega_s = \omega_0 - \omega_r$ is the slip velocity of electrical angle of motor.

Thus, in steady-state, the motor driving torque can be simplified to Eq. (28) (see, e.g. [26]). Then

the current i_{qs} takes the form as given in Eq. (29)

$$M_m = n_p l_m i_{ds} i_{qs}, \tag{28}$$

$$i_{qs} = \frac{M_m}{n_p l_m i_{ds}} = \frac{M_m}{n_p \psi_r}. \tag{29}$$

Substituting Eqs (27) and (29) into Eq. (25), yields the motor inner loss given in Eq. (30) (see, e.g. [41]) (Full derivation is given in Appendix C).

$$P_{is} = (a_1 + a_2 \omega_r^2)\psi_r^2 + a_3 (\frac{M_m}{\psi_r})^2, \tag{30}$$

where

$$a_1 = \frac{R_s}{l_m^2}, \quad a_2 = \frac{1}{R_r + R_{Fe}}, \quad a_3 = \frac{1}{n_p^2}(R_s + \frac{R_r R_{Fe}}{R_r + R_{Fe}}). \tag{31}$$

It can be concluded that P_{is} is a concave down function of ψ_r. Consequently, the optimized flux can be computed as:

$$\begin{aligned} &\frac{\partial P_{is}}{\partial \psi_r}|_{\psi_r = \psi_r^*} = 0, \\ &\psi_r^* = \sqrt{M_m} \sqrt[4]{\frac{a_3}{a_1 + a_2 \omega_r^2}}. \end{aligned} \tag{32}$$

According to Faraday's Law of Induction, an effective value of electromotive force generated in the stator windings of an induction motor can be expressed as (see, e.g. [39]):

$$U_e = \frac{2\pi}{\sqrt{2}} k_N f \psi_{max}. \tag{33}$$

where k_N is the stator winding coefficient; ψ_{max} is the maximum value of flux.

As described earlier, the leakage inductance of stator and rotor are ignored in this voltage regulation scheme, and thus the effective value of voltage can be simplified as the effective value of electromotive force in the stator windings. In this field-oriented frame, the three-phase alternating current is transformed into a two-phase direct current and $\psi_r = \sqrt{\frac{3}{2}} \psi_{max}$ is derived by the Park's Transformation (see, e.g. [42]). Therefore, the effective value of voltage can be expressed as:

$$U_m = U_e = \frac{2\sqrt{3}\pi}{3} k_N f \psi_r, \tag{34}$$

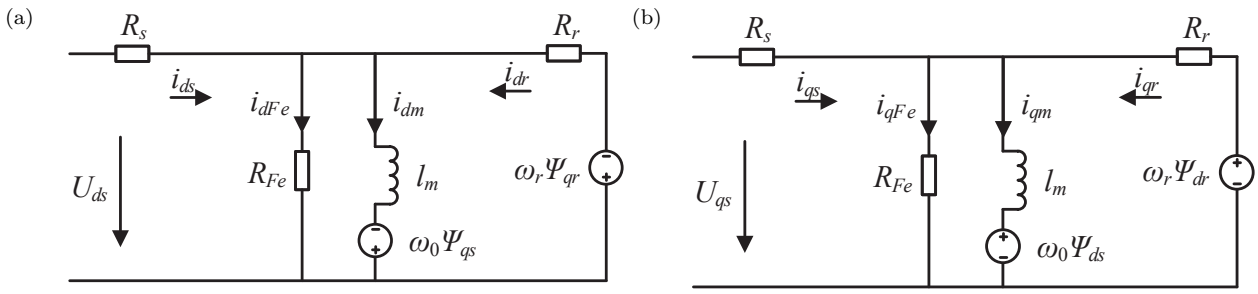

Figure 11: Steady state equivalent circuits of induction motor including an iron loss in the synchronously rotating frame and ignoring the leakage inductance of stator and rotator. (a) d-axis. (b) q-axis.

Substituting Eq. (32) into Eq. (34), the effective value of optimized voltage can be expressed as:

$$U_m^* = \frac{2\sqrt{3}\pi}{3} k_N f \sqrt{M_m} \sqrt[4]{\frac{a_3}{a_1 + a_2\omega_r^2}}. \tag{35}$$

6. Comparative analysis of the control schemes

This section presents a comparative analysis of the results obtained while the SRP is operated in one steady-state period using three different control schemes viz: (i) RTFOS; (ii) RTVRS; (iii) RTVFOS.

Real-Time Frequency Optimization Scheme

The dynamic responses of the SRP for (i) motor driven by the constant voltage and frequency (CFV) scheme and (ii) motor driven using real-time frequency optimization scheme (RTFOS) applying constant voltage and frequency ratio principle are presented in Fig. 12. In contrast to the CFV, the RTFOS provides a variable frequency curve to control the motor speed so that it matches with the load, and in the meanwhile it takes 588 s to complete this optimization process.

The following conclusions can be drawn from the simulated results:

- The peak value and standard deviation of motor output power are decreased by 18.37 % (from 29.40 kW to 24.00 kW) and 36.02 % (from 7.83 kW to 5.01 kW) respectively. This also leads to a significant reduction in the required motor rating (more than 5 kW in this case). Additionally, the average value of motor output power is the same as that of CFV (9.56 kW and 9.47 kW). This is due to the RTFOS only altering the instantaneous motor speed without changing the average speed in one period. This results in a "peak shaving and valley filling" of the load profile, effected by the inertial load redistribution.

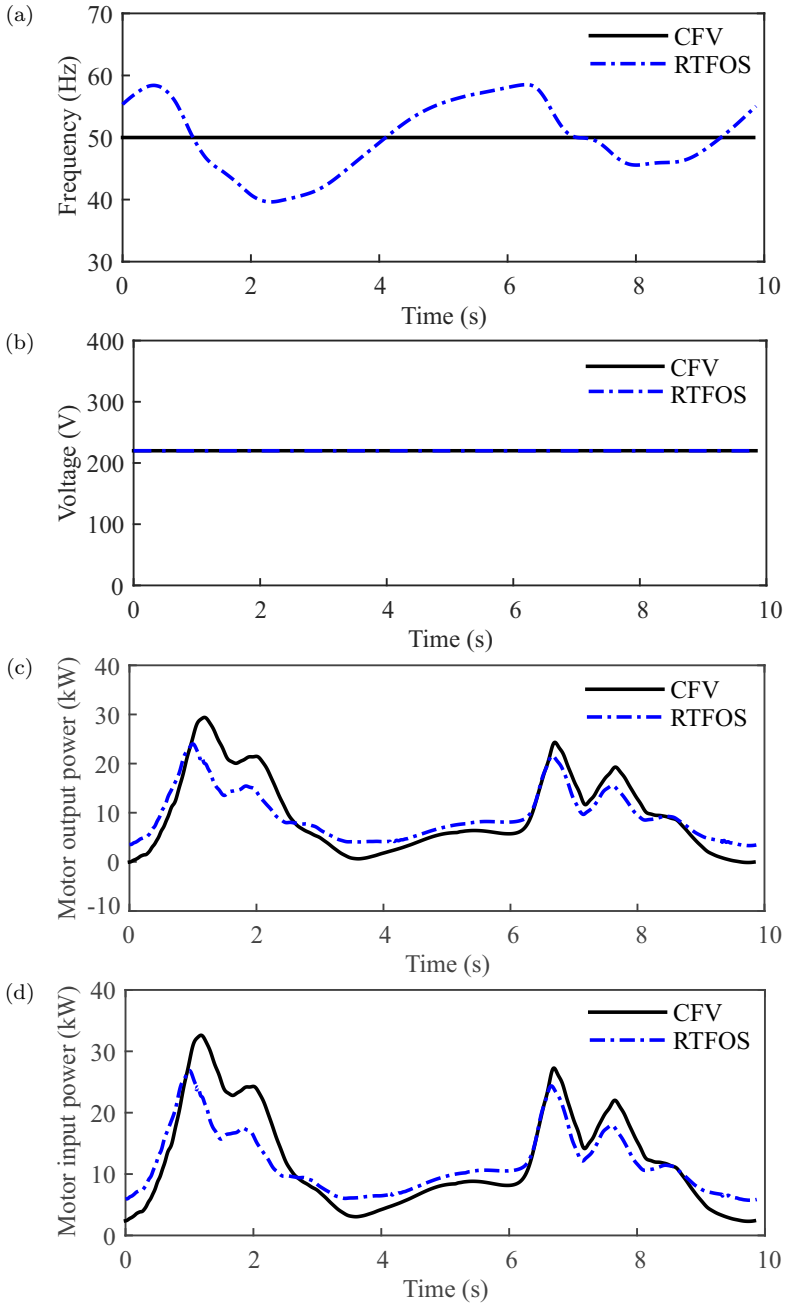

Figure 12: Comparisons of dynamic responses of SRP system for CFV and RTFOS. (a) Frequency varying from the constant power frequency supplied by CFV, RTFOS provides a real time variable frequency to match the load fluctuation. (b) Voltage of CFV and RTFOS; both supply constant voltage. (c) Motor output power shows that the RTFOS reduces the amplitude of output power and facilitates a lower rated motor to be employed. (d) Motor input power showing that the average input power is decreased causing by the RTFOS reduces the load fluctuation.

- The average value of motor input power is decreased by 3.53 % (from 12.19 kW to 11.76 kW). This energy saving originates from the reduction of the motor copper loss related to the load fluctuation. As the iron loss accounts for the largest proportion of the total electrical loss, the energy saving originating from motor copper loss is limited.

Real-Time Voltage Regulation Scheme

The dynamic responses of the SRP system for (i) motor driven by the constant voltage and frequency (CFV) scheme and (ii) motor driven using real-time voltage regulation scheme (RTVRS) with constant frequency are presented in Fig. 13. Compared to the CFV, the RTVRS presents a variable voltage to match the load variation that leads to a reduction in flux and consequently saves energy, and in the meanwhile it just takes 1 s to complete this optimization process.

As seen from the results, the motor output power is basically the same as in the CFV case, but the average value of motor input power is decreased by 12.88 % (from 12.19 kW to 10.62 kW). Thus the RTVRS results in significant energy saving without changing the original dynamic response of the SRP. This energy saving effect is in-line with the recorded experimental results (see, e.g. [22]), which show that the energy saved by employing the RTVRS is in the range of 4.07-11.95 %.

Real-Time Voltage and Frequency Optimization Scheme

The dynamic responses of the SRP system for (i) motor driven by the constant voltage and frequency (CFV) scheme and (ii) motor driven using real-time voltage and frequency optimization scheme (RTVFOS) are presented in Fig. 14. Compared to the CFV, the RTVFOS presents a real-time variable frequency and voltage matching with the load, and in the meanwhile it just takes 589 s to complete this optimization process. The following conclusions can be drawn from the simulated results:

- As the RTVFOS provides the best voltage based on operating status after applying the RTFOS and the RTFOS presents a good "peak shaving and valley filling" effect on the load, its voltage variation is less than that resulting from employing RTFOS as shown in Fig. 13b. As high (unaltered) voltage means lower current requirement for the same power output, this scheme results in lower heat generation (I^2R losses) and consequently slower thermal degradation of the motor - thereby leading to a longer operating life.

- The peak value and standard deviation of motor output power are decreased by 17.48 % (from 29.40 kW to 24.26 kW) and 36.91 % (from 7.83 kW to 4.94 kW) respectively. Compared to the

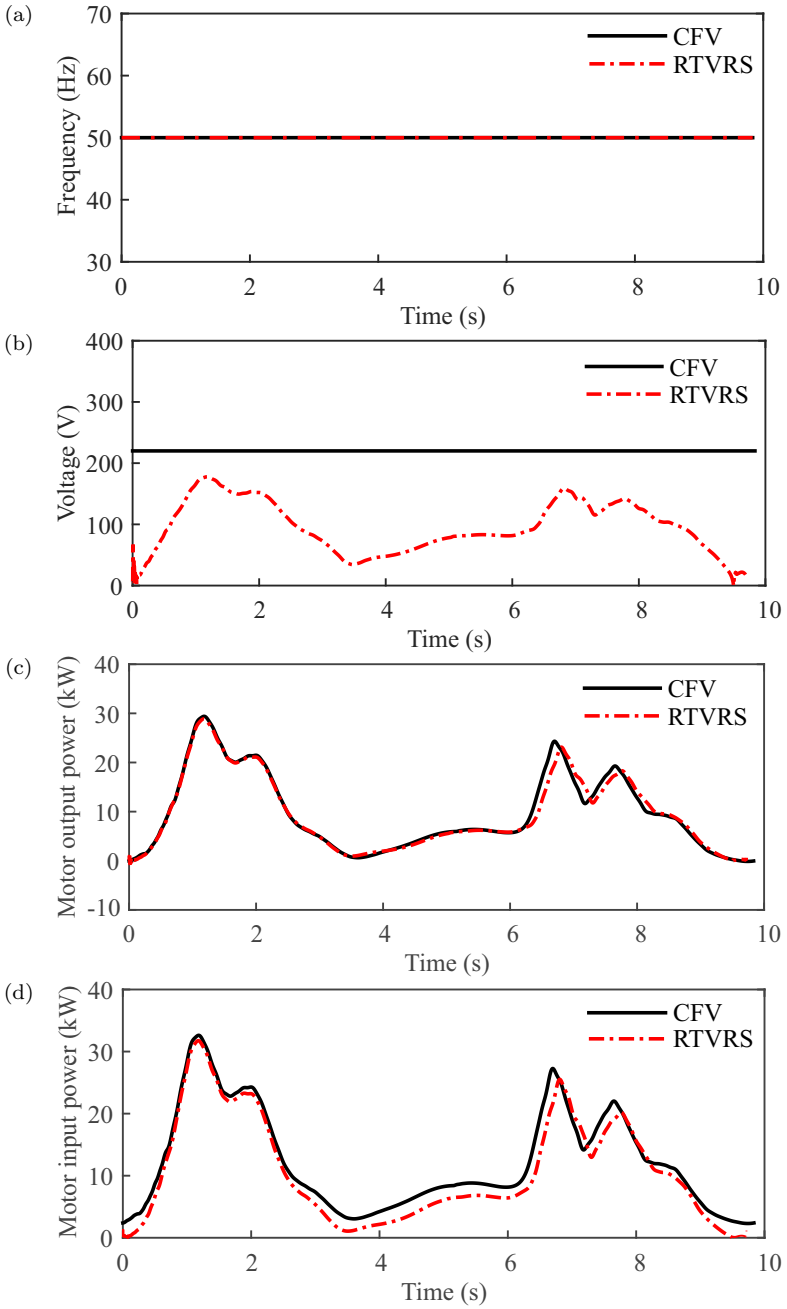

Figure 13: Comparisons of dynamic responses of SRP system for CFV and RTVRS. (a) Frequency of CFV and RTVRS; both supply constant frequency. (b) Voltage varying from the constant voltage effective value supplied by CFV, RTVRS provides a real time variable voltage effective value to match the load fluctuation. (c) Motor output power shows that the voltage regulation barely affect the SRP dynamic response. (d) Motor input power showing that the RTVRS presents an obvious reduction on the average input power with decreasing the iron loss by regulating voltage.

results shown in Fig. 12c, the RTVFOS delivers basically identical system dynamic response as that of RTFOS.

- The average value of motor input power is decreased by 13.95 % (from 12.19 kW to 10.49 kW). Therefore, the energy savings delivered by RTVFOS are greater than both RTFOS and RTVRS.

Based on the above simulated results and analysis, the RTVFOS proposed in this paper possesses the combined advantages of both RTFOS and RTVRS viz: (i) Smoother load fluctuation, reducing motor rating and consequently motor copper loss, (ii) Voltage regulation results in reducing the extra flux and saving energy. More importantly, the RTVFOS reduces the voltage amplitude range compared to RTVRS, which is favourable in prolonging the operating life of the employed motor. To further demonstrate this conclusion, the simulated comparison results of four additional oil wells within the Changqing Oilfield are listed in Table. 3. The results agree well with the above conclusions. After applying the RTVFOS, reduction on load variation is in the range of 30.92 %-37.93 %, motor rating reduction is in the range of 12.35 %-31.41 % and energy saving is in the range of 7.70 %-18.97 %.

Fig. 15 depicts the physical computing time of CFV, RTFOS, RTVRS and RTVFOS for all the testing oil wells in this paper. The average physical computing time of CFV, RTFOS, RTVRS and RTVFOS is 1 s, 579 s, 1 s and 580 s, respectively. The basic parameters of an oil well vary very slowly, especially while the swabbing parameters matching well with the fluid supply by the formation. However, the oil well parameters in the SQL database need 1200 s to complete overall update in the Changqing Oilfield. Therefore, the computing time of optimization scheme should be within this restrict of time and our control scheme apparently can satisfy the current field requirements.

7. Conclusions

To analyze the dynamic response and evaluate the energy consumption of sucker-rod pumping (SRP) system, a coupled electro-mechanical model for this system is proposed and validated. The model is expressed as a set seventeen first-order ordinary differential equations and solved numerically, where both transient and steady-state responses were analyzed. The field-recorded data from a surface dynamometer card and motor input power is used for validating this simulation model. Results show that this model can meet the practice requirement.

A real-time voltage and frequency optimization scheme (RTVFOS) is proposed and tested on the system model. These results are then compared with the constant voltage and frequency (CFV) scheme, real-time frequency optimization scheme (RTFOS) applying constant voltage and frequency

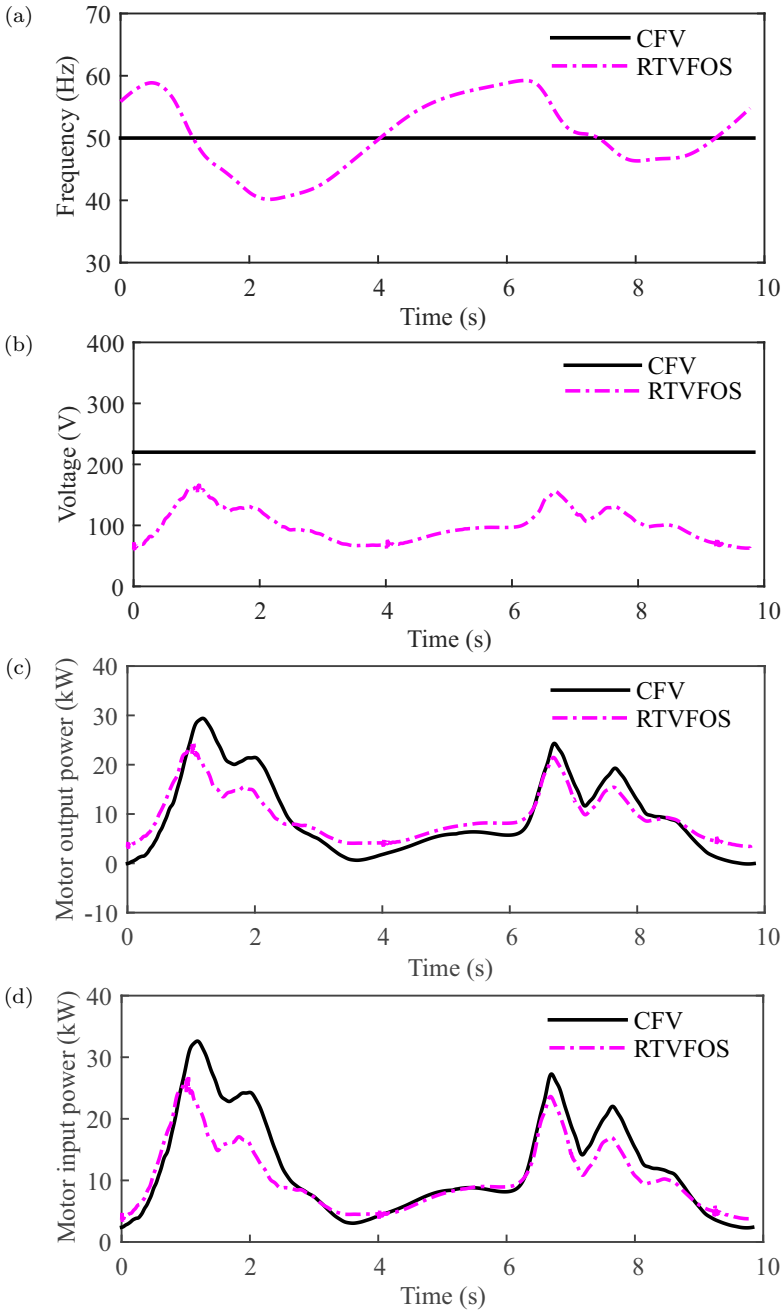

Figure 14: Comparisons of dynamic responses of SRP system for CFV and RTVFOS. (a) Frequency varying from the constant power frequency supplied by CFV, RTVFOS provides a real-time variable frequency to match the load fluctuation. (b) Voltage varying from the constant voltage effective value supplied by CFV, RTVFOS provides a real-time variable voltage effective value to match the load. (c)Motor output power shows that the RTVFOS reduces the amplitude of output power and facilitates a lower rated motor to be employed. (d) Motor input power showing that the RTVFOS presents an obvious reduction on the average input power with decreasing the iron loss by regulating voltage.

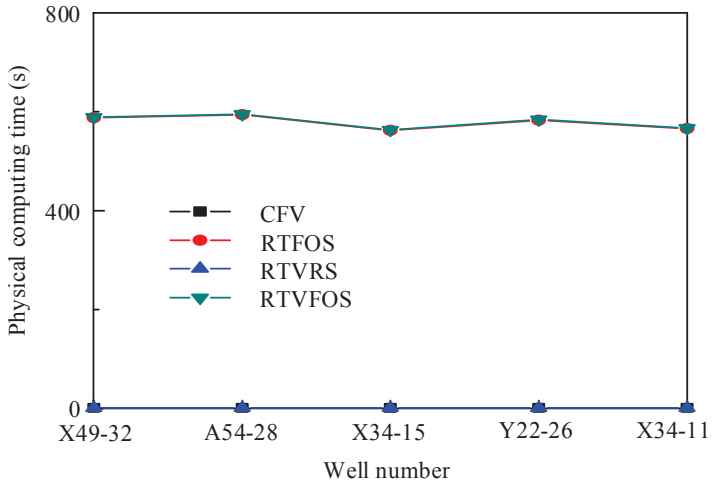

Figure 15: Physical computing time of CFV, RTFOS, RTVRS and RTVFOS for each well.The CFV and RTVRS complete the computing time within 1 s, whereas RTFOS and RTVFOS consume much more time as the genetic algorithm is employed.

Table 3: Results comparison of three control schemes

Well number		RTFOS	RTVRS	RTVFOS
A54-28	**Frequency amplitude (Hz)**	23.55	0	23.55
	Voltage amplitude (V)	0	187.74	111.03
	Motor rating reduction (%)	21.93	0.64	21.93
	Reduction on standard deviation of motor output power (%)	35.44	1.22	35.49
	Energy saving (%)	3.71	9.69	10.87
	Physical computing time (s)	594	1	595
X34-15	**Frequency amplitude (Hz)**	26.85	0	26.85
	Voltage amplitude (V)	0	189.74	114.09
	Motor rating reduction (%)	12.24	2.53	12.35
	Reduction on standard deviation of motor output power (%)	30.52	1.66	30.92
	Energy saving (%)	3.25	9.76	10.42
	Physical computing time (s)	562	1	563
Y22-26	**Frequency amplitude (Hz)**	29.67	0	29.67
	Voltage amplitude (V)	0	159.79	108.59
	Motor rating reduction (%)	30.99	2.13	31.41
	Reduction on standard deviation of motor output power (%)	33.29	1.24	33.67
	Energy saving (%)	7.91	17.49	18.97
	Physical computing time (s)	583	1	584
X34-11	**Frequency amplitude (Hz)**	19.29	0	19.29
	Voltage amplitude (V)	0	197.39	108.59
	Motor rating reduction (%)	19.56	0.59	19.76
	Reduction on standard deviation of motor output power (%)	37.83	1.14	37.93
	Energy saving (%)	2.71	6.66	7.70
	Physical computing time (s)	566	1	567

ratio principle and real-time voltage regulation scheme (RTVRS) with constant frequency. Through a comparative analysis of the simulation results, it is shown that the RTFOS reduces the load fluctuation by redistributing the inertial load. Furthermore, the RTVRS delivers significant energy saving. However, the RTVFOS combines the advantages of both the schemes, reducing the motor rating by 12.35 %-31.41 % and saving the energy by 7.70 %-18.97 %. A practical implementation and validation of the proposed control scheme will be pursued in the immediate future.

Acknowledgments

The research in this paper is supported and funded by programs with China Scholarship Council (Grant 201708130108), Natural Science Foundation of Hebei Province (Grant E2017203101), and National Natural Science Foundation of China (Grant 51974276).

Declarations of interest

There is no conflict of interest for all contributing authors.

Appendix A. Equivalent resistive torque of the crank

Referring to Fig. 4, we take moment about point D and the axial force of the pitman is derived,

$$F_P = \frac{1}{L_C \sin\beta}(F_{RL}L_A - G_3L_3\sin(\theta_4-\alpha)) = \frac{1}{L_C \sin(\theta_4-\theta_3)}(F_{RL}L_A - G_3L_3\sin(\theta_4-\alpha)), \tag{A.1}$$

and then the tangential force from the pitman acting on the crank is given,

$$F_t = -F_P\sin\gamma + G_2\sin(2\pi-\theta_1) = -F_P\sin(\theta_2-\theta_3) - G_2\sin\theta_1. \tag{A.2}$$

Therefore, the equivalent resistive torque of the crank is expressed by Eq. (A.3) on which Eqs. (A.1) and (A.2) are substituted into.

$$\begin{aligned} M_{ec} =& F_tL_R + G_1L_1\sin(\theta_2-\alpha) + G_1'L_R\sin(\theta_2-\alpha+\tau), \\ =& \left[-\frac{\sin(\theta_2-\theta_3)}{L_C\sin(\theta_4-\theta_3)}(F_{RL}L_A - G_3L_3\sin(\theta_4-\alpha)) - G_2\sin\theta_1\right]L_R \\ &+ G_1L_1\sin(\theta_2-\alpha) + G_1'L_R\sin(\theta_2-\alpha+\tau). \end{aligned} \tag{A.3}$$

For the ease of modelling the system, the variables in Eq. (A.3) are initialized as follows:

$$\alpha = \arcsin(\frac{L_I}{L_K}), \quad \theta_1 = \frac{\theta_m}{\varepsilon_{mc}} - \theta_0, \quad \theta_2 = 2\pi - \theta_1 + \alpha, \quad \theta_3 = \arccos(\frac{L_P^2 + L_L^2 - L_C^2}{2L_P L_L}) - \arcsin(\frac{L_R}{L_L}\sin\theta_2),$$
$$\theta_4 = \pi - \arccos(\frac{L_L^2 + L_C^2 - L_P^2}{2L_C L_L}) - \arcsin(\frac{L_R}{L_L}\sin\theta_2). \tag{A.4}$$

The length, L_L, and the initial angle of the crank, θ_0, can be expressed as:

$$L_L = \sqrt{L_R^2 + L_K^2 - 2L_R L_K \cos\theta_2}, \quad \theta_0 = \arccos(\frac{(L_P + L_R)^2 + L_K^2 - L_C^2}{2(L_P + L_R)L_K}) - \arcsin(\frac{L_I}{L_K}), \tag{A.5}$$

Appendix B. Mathematical model

The voltage equations given in Eq. (1) can be expressed into the state equations for an induction motor, as follows:

$$\begin{pmatrix} \psi'_{dr} \\ \psi'_{qr} \\ i'_{ds} \\ i'_{qs} \\ i'_{dm} \\ i'_{qm} \end{pmatrix} = \begin{pmatrix} -\frac{R_r}{l_{lr}} & \omega_0 - \omega_r & 0 & 0 & \frac{R_r l_m}{l_{lr}} & 0 \\ \omega_r - \omega_0 & -\frac{R_r}{l_{lr}} & 0 & 0 & 0 & \frac{R_r l_m}{l_{lr}} \\ -\frac{R_{Fe}}{l_{ls} l_{lr}} & 0 & -\sigma_1 & \omega_0 & \frac{\sigma_2}{l_{ls}} & 0 \\ 0 & -\frac{R_{Fe}}{l_{ls} l_{lr}} & -\omega_0 & -\sigma_1 & 0 & \frac{\sigma_2}{l_{ls}} \\ \frac{R_{Fe}}{l_{lr} l_m} & 0 & \frac{R_{Fe}}{l_m} & 0 & -\frac{\sigma_2}{l_m} & \omega_0 \\ 0 & \frac{R_{Fe}}{l_{lr} l_m} & 0 & \frac{R_{Fe}}{l_m} & -\omega_0 & -\frac{\sigma_2}{l_m} \end{pmatrix} \begin{pmatrix} \psi_{dr} \\ \psi_{qr} \\ i_{ds} \\ i_{qs} \\ i_{dm} \\ i_{qm} \end{pmatrix} + \begin{pmatrix} 0 \\ 0 \\ \frac{U_{ds}}{l_{ls}} \\ \frac{U_{qs}}{l_{ls}} \\ 0 \\ 0 \end{pmatrix}, \tag{B.1}$$

where $\sigma_1 = \frac{R_s + R_{Fe}}{l_{ls}}$; $\sigma_2 = \frac{R_{Fe}(l_m + l_{lr})}{l_{lr}}$.

Equation of motion for the surface transmission system given in Eq. (9) can be expressed as

$$\begin{aligned} \theta'_m &= \omega_m, \\ \omega'_m &= \frac{1}{J_e}(M_m - M_{eq} - \frac{1}{2}\theta'_m J'_e). \end{aligned} \tag{B.2}$$

where ω_m is the velocity of the mechanical angle of motor.

To solve the rod string longitudinal vibration equation given in Eq. (12), the forced vibration solution is expressed as the sum of all modes of vibration,

$$u(x,t) = \sum_{i=1}^{\infty} \phi_i(x) q_i(t). \tag{B.3}$$

where $\phi_i(x)$ is the i-th mode shape and $q_i(t)$ is the i-th modal coordinate.

As the natural frequency and mode shape is the intrinsic properties of a rod string having nothing to do with the condition, they are generally solved while the rod string suffers a free vibration with the absence of damping. The rod string free longitudinal vibration equation is written as,

$$\begin{aligned} \frac{\partial^2 u(x,t)}{\partial x^2} &= \frac{1}{c^2}\frac{\partial^2 u(x,t)}{\partial t^2}, \\ u(0,t) &= 0, \\ \frac{\partial u(L_r,t)}{\partial x} &= 0, \end{aligned} \tag{B.4}$$

where $c = \sqrt{\frac{E_r}{\rho_r}}$ is the velocity of vibration wave propagation along the rod string.

With the principle of separation of variables, the solution of Eq. (B.4) is written as

$$u(x,t) = \phi(x)q(t) = [A\sin\frac{p_n}{c}x + B\cos\frac{p_n}{c}x]\sin(p_n t + \varphi), \tag{B.5}$$

where p_n is the natural frequency of the rod string; the constant A, B and p_n are determined from the boundary conditions and initial conditions.

With the boundary conditions in Eq. (B.4), the i-th mode shape and natural frequency are derived as,

$$\phi_i(x) = d_1\sin(\frac{(2i-1)\pi}{2L_r}x),\ p_{ni} = \frac{(2i-1)\pi c}{2L_r}. \tag{B.6}$$

The general form of Eq. (12) can be expressed as,

$$A_r\rho_r\frac{\partial^2 u(x,t)}{\partial t^2} - E_r A_r\frac{\partial^2 u(x,t)}{\partial x^2} + \upsilon\frac{\partial u(x,t)}{\partial t} = f(x,t), \tag{B.7}$$

where $f(x,t)$ is the time-varying external force per unit length.

With Eq. (B.3) is taken into Eq. (B.7), it is written as

$$\sum_{i=1}^{\infty} A_r\rho_r\phi_i(x)q_i''(t) - \sum_{i=1}^{\infty} A_r E_r\phi_i''(x)q_i(t) + \sum_{i=1}^{\infty}\upsilon\phi_i(x)q_i'(t) = f(x,t), \tag{B.8}$$

Multiplying Eq. (B.8) by $\phi_i(x)$ and integrating over the rod string length, Eq. (B.9) is derived by the mode shape orthogonality,

$$A_r\rho_r M q_i''(t) + \upsilon M q_i'(t) - E_r A_r K q_i(t) = \int_0^{L_r}\phi_i(x)f(x,t)dx, \tag{B.9}$$

where

$$M = \int_0^{L_r} \phi_i^2(x)dx,\ K = \int_0^{L_r} \phi_i(x)\phi_i''(x)dx. \tag{B.10}$$

Putting Eq. (B.6) into Eq. (B.10) yields,

$$M = \frac{d_1^2 L_r \rho_r A_r}{2},\ K = \frac{p_{ni}\rho_r}{E_r}\int_0^{L_r} \phi_i^2(x)dx = \frac{p_{ni}\rho_r}{E_r}M, \tag{B.11}$$

Eq. (B.9) can then be rewritten as follows when normalized with respect to the mass, M,

$$q_i''(t) + \frac{\upsilon}{A_r\rho_r}q_i'(t) - p_{ni}^2 q_i(t) = F_i, \tag{B.12}$$

where

$$F_i = (u_a'' + \frac{\upsilon}{A_r\rho_r}u_a')\frac{2\sqrt{2A_r\rho_r L_r}}{(2i-1)\pi} + F_{PL}\sqrt{\frac{2}{A_r\rho_r L_r}}\sin(\frac{(2i-1)\pi}{2}). \tag{B.13}$$

The Eq. (B.12) is expressed as the first order differential equations in order to solve it (it is expanded to the fourth order, which can satisfy the calculation accuracy),

$$\begin{aligned}
&x_{11}' = x_{12},\\
&x_{12}' = -\frac{\upsilon}{\rho_r A_r}x_{12} - \frac{E_r}{\rho_r}(\frac{\pi}{2L_r})^2 x_{11} + (u_a'' + \frac{\upsilon}{\rho_r A_r}u_a')\frac{2\sqrt{2A_r\rho_r L_r}}{\pi} + F_{PL}\sqrt{\frac{2}{A_r\rho_r L_r}}\sin(\frac{\pi}{2}),\\
&x_{21}' = x_{22},\\
&x_{22}' = -\frac{\upsilon}{\rho_r A_r}x_{22} - \frac{E_r}{\rho_r}(\frac{3\pi}{2L_r})^2 x_{21} + (u_a'' + \frac{\upsilon}{\rho_r A_r}u_a')\frac{2\sqrt{2A_r\rho_r L_r}}{3\pi} + F_{PL}\sqrt{\frac{2}{A_r\rho_r L_r}}\sin(\frac{3\pi}{2}),\\
&x_{31}' = x_{32},\\
&x_{32}' = -\frac{\upsilon}{\rho_r A_r}x_{32} - \frac{E_r}{\rho_r}(\frac{5\pi}{2L_r})^2 x_{31} + (u_a'' + \frac{\upsilon}{\rho_r A_r}u_a')\frac{2\sqrt{2A_r\rho_r L_r}}{5\pi} + F_{PL}\sqrt{\frac{2}{A_r\rho_r L_r}}\sin(\frac{5\pi}{2}),\\
&x_{41}' = x_{42},\\
&x_{42}' = -\frac{\upsilon}{\rho_r A_r}x_{42} - \frac{E_r}{\rho_r}(\frac{7\pi}{2L_r})^2 x_{41} + (u_a'' + \frac{\upsilon}{\rho_r A_r}u_a')\frac{2\sqrt{2A_r\rho_r L_r}}{7\pi} + F_{PL}\sqrt{\frac{2}{A_r\rho_r L_r}}\sin(\frac{7\pi}{2}),
\end{aligned} \tag{B.14}$$

where $x_{i1} = q_i(t)$ and $x_{i2} = q_i'(t)$, $i = 1, 2, 3, 4$.

Therefore, the polished rod load is expressed as,

$$\begin{aligned}
F_{RL} &= E_r A_r \frac{\partial u(x,t)}{\partial x}|_{x=0} + G_r = E_r A_r \frac{\partial(\sum_{i=1}^4 \phi_i(x)q_i(t))}{\partial x}|_{x=0} + G_r,\\
&= \frac{E_r A_r \pi}{L_r}\sqrt{\frac{2}{A_r\rho_r L_r}}(\frac{1}{2}x_{11} + \frac{3}{2}x_{21} + \frac{5}{2}x_{31} + \frac{7}{2}x_{41}) + G_r.
\end{aligned} \tag{B.15}$$

where G_r is the weight of the rod string.

For the pumping model Eq. (15), it can be expressed as

$$p' = \begin{cases} \dfrac{v_p A_p p_d}{V_{og}(-1/n)(p/p_d)^{-\frac{1}{n}-1}}, & \text{stage 1 : if } v_p > 0 \quad \text{and} \quad p > p_s \\ 0, & \text{stage 2 : if } v_p > 0 \quad \text{and} \quad p = p_s \\ \dfrac{v_p A_p p_s}{V_g(-1/n)(p/p_s)^{-\frac{1}{n}-1}}, & \text{stage 3 : if } v_p < 0 \quad \text{and} \quad p < p_d \\ 0. & \text{stage 4 : if } v_p < 0 \quad \text{and} \quad p = p_d \end{cases} \tag{B.16}$$

The polished rod displacement is taken as a reference shown in Fig. 5, and then the plunger displacement, u_p, is written as,

$$u_p = u_a - u(L_r, t) = u_a - \sum_{i=1}^{4} \phi_i(L_r) q_i(t) = u_a - \sqrt{\frac{2}{A_r \rho_r L_r}}(x_{11} - x_{21} + x_{31} - x_{41}), \tag{B.17}$$

and then the plunger velocity, v_p, is given as,

$$v_p = u_a' - \sqrt{\frac{2}{A_r \rho_r L_r}}(x_{12} - x_{22} + x_{32} - x_{42}). \tag{B.18}$$

By combining Eq. (B.1), Eq. (B.2), Eq. (B.14) and Eq. (B.16), the numerical model of SRP system is established with seventeen state variables $\boldsymbol{X} = [\psi_{dr}, \psi_{qr}, i_{ds}, i_{qs}, i_{dm}, i_{qm}, \theta_m, \omega_m, x_{11}, x_{12}, x_{21}, x_{22}, x_{31}, x_{32}, x_{41}, x_{42}, p]$, and the flow chart for solving the SRP system model is given in Fig. B.1

Appendix C. Motor inner loss

The expression of rotor current in q axis is given in Eq. (27), and then the ω_s can expressed as

$$\omega_s = -\frac{R_r}{\psi_r} i_{qr} = \frac{R_r}{\psi_r}(i_{qs} - i_{qFe} - i_{qm}) = \frac{R_r}{\psi_r}(i_{qs} - \frac{\omega_1}{R_{Fe}}\psi_r) = \frac{R_r}{\psi_r}(i_{qs} - \frac{(\omega_s + \omega_r)}{R_{Fe}}\psi_r), \tag{C.1}$$

and ω_s is derived as:

$$\omega_s = (\frac{i_{qs}}{\psi_r} - \frac{\omega_r}{R_{Fe}})\frac{R_r R_{Fe}}{R_r + R_{Fe}}. \tag{C.2}$$

Substituting Eqs (27) and (C.2) into Eq. (26), the stator copper loss, P_{Cus}, rotor copper loss, P_{Cur} and iron loss, P_{Fe} can be derived as:

$$P_{Cus} = (i_{ds}^2 + i_{qs}^2)R_s = ((\frac{\psi_r}{L_m})^2 + i_{qs}^2)R_s, \tag{C.3}$$

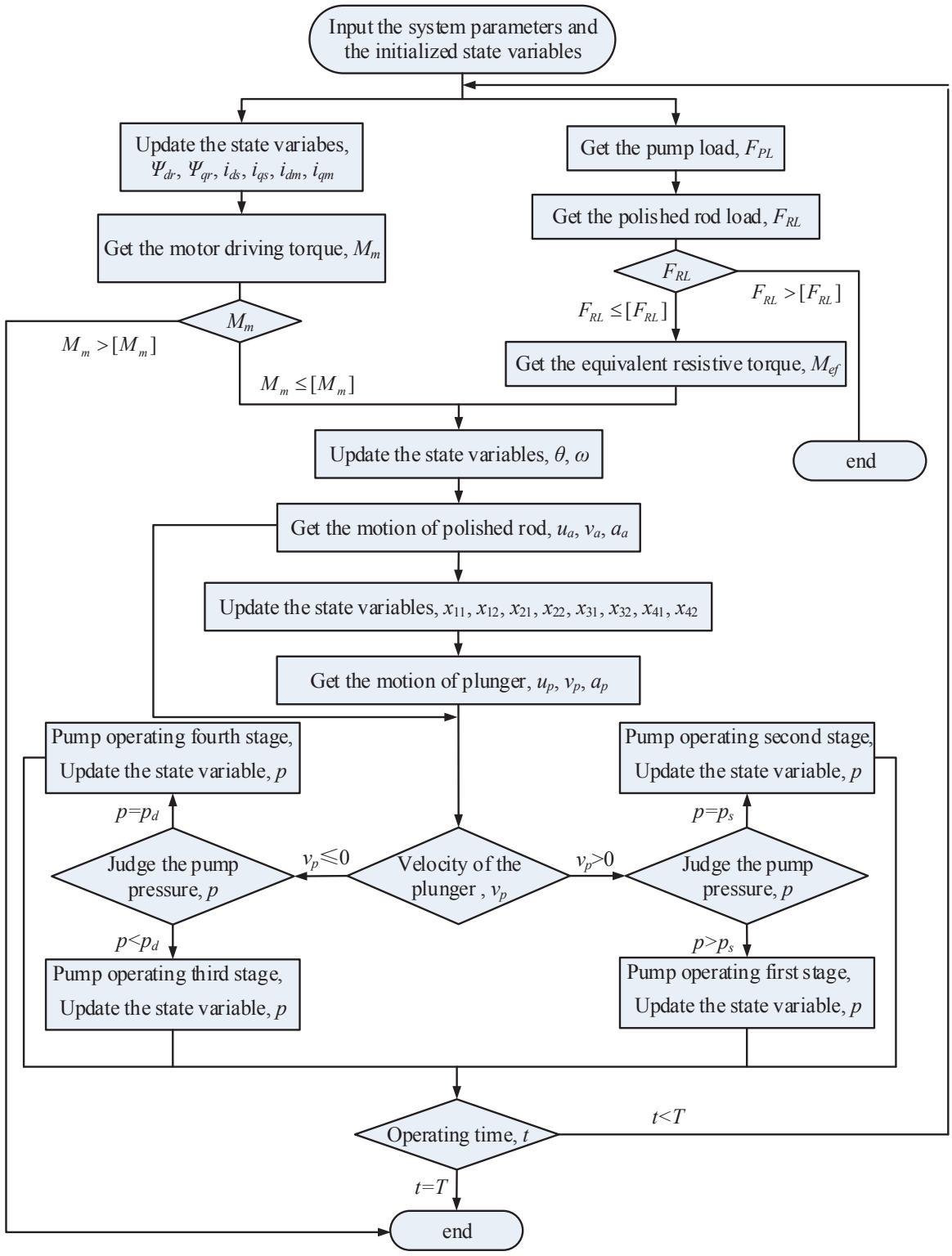

Figure B.1: The flow chart for solving the SRP system model in one period. The initialized system parameters and state variables are taken as the inputs, and the state variables are updated over time, by applying the state equations of motor, surface transmission model and downhole pumping model in sequence. This cyclic iterative process terminates after one SRP operating period.

$$P_{Cur} = (i_{dr}^2 + i_{qr}^2)R_r = i_{qr}^2 R_r = (-\frac{\omega_s}{R_r}\psi_r)^2 R_r = (i_{qs}R_{Fe} - \omega_r\psi_r)^2 \frac{R_r}{(R_r + R_{Fe})^2}, \tag{C.4}$$

$$\begin{aligned} P_{Fe} &= (i_{dFe}^2 + i_{qFe}^2)R_{Fe} = i_{qFe}^2 R_{Fe} = (\frac{\omega_1}{R_{Fe}}\psi_r)^2 R_{Fe} = (\frac{\omega_s + \omega_r}{R_{Fe}}\psi_r)^2 R_{Fe} \\ &= (i_{qs}R_r + \omega_r\psi_r)^2 \frac{R_{Fe}}{(R_r + R_{Fe})^2}. \end{aligned} \tag{C.5}$$

Putting the expression of i_{qs} given in Eq. (29) into Eqs (C.3), (C.4) and (C.5), the motor inner loss, P_{is} is derived as:

$$P_{is} = P_{Cus} + P_{Cur} + P_{Fe} = (\frac{R_s}{l_m^2} + \frac{\omega_r^2}{R_r + R_{Fe}})\psi_r^2 + \frac{1}{n_p^2}(R_s + \frac{R_r R_{Fe}}{R_r + R_{Fe}})(\frac{M_m}{\psi_r})^2. \tag{C.6}$$

Appendix D. Nomenclature

A_p	Cross-section area of the plunger [m^2]
A_r	Cross-section area of the rod string [m^2]
a_0, a_j, b_j	Fourier coefficients
c	Velocity of the vibration wave propagation along the rod string [m/s]
E_r	Elastic modulus of the rod string [Pa]
F_{PL}	Pump load [N]
F_{RL}	Polished rod load [N]
f	Motor driving frequency [Hz]
G_1	Weight of the crank [N]
G_1'	Weight of counter-weight [N]
G_2	Weight of the pitman [N]
G_3	Weight of the walking beam [N]
G_r	Weight of the rod string [N]
g	Gravitational acceleration [m/s^2]
i_{dm}, i_{qm}	Field current in d-axis and q-axis, respectively [A]
i_{dr}, i_{qr}	Rotator current in d-axis and q-axis, respectively [A]
i_{ds}, i_{qs}	Stator current in d-axis and q-axis, respectively [A]
J_e	Equivalent moment of inertia of the surface transmission system [kg m^2]
J_i	Moment of inertia of the i-th component in this surface transmission system [kg m^2]
L_r	Length of rod string [m]
L_p	Pump setting depth [m]
l_{lr}	Rotor leakage inductance [H]
l_{ls}	Stator leakage inductance [H]
l_m	Mutual inductance between stator and rotor [H]
M_m	Motor driving torque [Nm]
M_{eq}	Equivalent resistive torque of the motor [Nm]
M_{ec}	Equivalent resistive torque of the crank [Nm]
m_i	Mass of the i-th component in this surface transmission system [kg]
n	Gas polytropic exponent
n_p	Number of motor pole-pairs
P_{Cur}	Rotor copper loss [W]
P_{Cus}	Stator copper loss [W]
P_{Fe}	Iron loss [W]
P_{std}	Standard deviation of motor output power [W]
p	Pressure in the pump cylinder [Pa]
p_d	Pump outlet pressure [Pa]
p_s	Pump intake pressure [Pa]

p_t	Tubing head pressure [Pa]
R_{Fe}	Iron core resistance [Ω]
R_r	Rotor resistance [Ω]
R_s	Stator resistance [Ω]
T	Operating period of the SRP system [s]
U_i	Phase voltage, $i = a, b, c$ [V]
U_m	Effective value of the voltage [V]
U_e	Effective value of electromotive force in the stator windings [V]
u_a	Polished rod position [m]
$u(x, t)$	Displacement of the rod string at an arbitrary depth and time [m]
V_g	Gas volume in the pump when plunger arrives at the top of the stroke [m^3]
V_p	Pump stroke volume [m^3]
V_{og}	Gas volume in the pump when plunger arrives at the bottom of the stroke [m^3]
V_x	Pump displacement volume [m^3]
v_a	Velocity of the polished rod [m/s]
v_i	Velocity of the centre of mass of the i-th component in this surface transmission system [m/s]
ε_{mc}	Transmission ratio from the motor to the crank
η_{mc}	Transmission efficiency from the motor to the crank
η_{cp}	Transmission efficiency from the crank to the polished rod
η_w	Water content
θ_0	Initial angle of the crank [rad]
θ_m	Mechanical angle of the motor [rad]
θ_{m0}	Initial angle of the motor [rad]
θ_s	Rotating angle of the d-q coordinate system [rad]
ρ_r	Density of the rod string [kg/m^3]
ρ_o	Density of the oil [kg/m^3]
ρ_w	Density of the water [kg/m^3]
τ	Offset angle of the counter-weight [rad]
υ	Liquid-to-rod string damping coefficient [Pa s]
φ_i	Phase angle of the voltage, $\varphi_i = 0, -\frac{2}{3}\pi, -\frac{4}{3}\pi$ while $i = a, b, c$, respectively [rad]
ψ_{dr}, ψ_{qr}	Rotor flux in d-axis and q-axis, respectively [Wb]
ψ_{max}	Maximum value of flux [Wb]
ω_0	Synchronous velocity of the electric angle of motor [rad/s]
ω_i	Angular velocity of the i-th component in this surface transmission system [rad/s]
ω_m	Velocity of the mechanical angle of motor [rad/s]
ω_n	Rated value of the angular velocity of motor [rad/s]
ω_r	Velocity of the electric angle of motor [rad/s]

References

[1] L. M. Lao and H. Zhou, "Application and effect of buoyancy on sucker rod string dynamics," *Journal of Petroleum Science and Engineering*, vol. 146, pp. 264–271, 2016.

[2] D. Y. Wang and L. H. Zhao, "Prediction and analysis of polished rod dynamometer card in sucker rod pumping system with wear," *Shock and Vibration*, vol. 2018, pp. 1–10, 2018.

[3] W. Liang, X. C. Yu, L. B. Zhang, and W. Q. Lu, "Self-organization comprehensive real-time state evaluation model for oil pump unit on the basis of operating condition classification and recognition," *Mechanical Systems and Signal Processing*, vol. 104, pp. 224 – 241, 2018.

[4] B. Y. Zheng, X. W. Gao, and X. Y. Li, "Diagnosis of sucker rod pump based on generating dynamometer cards," *Journal of Process Control*, vol. 77, pp. 76–88, 2019.

[5] T. A. Aliev, O. G. Nusratov, G. Guluyev, A. G. Rzaev, F. G. Pashaev, and M. G. Rezvan, "Position-binary technology for processing the signals of a load for identification of the technical state of deep-well sucker-rod pumps," *Measurement Techniques*, vol. 61, no. 9, pp. 885–890, 2018.

[6] H. Q. Lv, J. Liu, J. Q. Han, and A. Jiang, "An energy saving system for a beam pumping unit," *Sensors*, vol. 16, no. 5, pp. 1–13, 2016.

[7] M. M. Xing and S. M. Dong, "A new simulation model for a beam-pumping system applied in energy saving and resource-consumption reduction," *SPE Production & Operations*, vol. 30, no. 2, pp. 130–140, 2015.

[8] T. Gabor, *Sucker-rod pumping handbook: production engineering fundamentals and long-stroke rod pumping*. Gulf Professional Publishing, 2015.

[9] X. F. Liu and Y. G. Qi, "A modern approach to the selection of sucker rod pumping systems in cbm wells," *Journal of Petroleum Science and Engineering*, vol. 76, no. 3-4, pp. 100–108, 2011.

[10] L. Firu, T. Chelu, and C. Militaru-Petre, "A modern approach to the optimum design of sucker-rod pumping system," in *SPE Annual Technical Conference and Exhibition*, Society of Petroleum Engineers, 2003.

[11] T. Aliev, A. Rzayev, G. Guluyev, T. Alizada, and N. Rzayeva, "Robust technology and system for management of sucker rod pumping units in oil wells," *Mechanical Systems and Signal Processing*, vol. 99, no. 15, pp. 47–56, 2018.

[12] W. C. Li, S. M. Dong, and X. R. Sun, "An improved sucker rod pumping system model and swabbing parameters optimized design," *Mathematical Problems in Engineering*, vol. 2018, pp. 1–15, 2018.

[13] H. S. Zhao, Y. L. Wang, Y. Zhan, G. R. Xu, X. S. Cui, and J. Wang, "Practical model for energy consumption analysis of beam pumping motor systems and its energy-saving applications," *IEEE Transactions on Industry Applications*, vol. 54, no. 2, pp. 1006–1016, 2018.

[14] Z. M. Feng, H. H. Ding, and M. Z. Jiang, "New secondary balancing method saves energy for crank-balanced rod-pumping application," *SPE Production & Operations*, vol. 30, no. 2, pp. 141–145, 2015.

[15] Z. M. Feng, J. J. Tan, Q. Li, and X. Fang, "A review of beam pumping energy-saving technologies," *Journal of Petroleum Exploration and Production Technology*, vol. 8, no. 1, pp. 299–311, 2018.

[16] X. P. Li, K. Tian, C. H. Li, Y. Zhou, L. Y. Li, and J. J. Hong, "Liner electromagnetic oil pumping unit based on the principle of coil gun," *IEEE Transactions on Magnetics*, vol. 45, no. 1, pp. 951–961, 2009.

[17] S. G. Gibbs, "Computing gearbox torque and motor loading for beam pumping units with consideration of inertia effects," *Journal of Petroleum Technology*, vol. 27, no. 9, pp. 1153–1159, 1975.

[18] W. M. Rossini, B. Alvarenga, I. E. Chabu, J. J. da Cruz, J. R. Cardoso, and R. M. Sales, "New concept for lifting in onshore oil wells," *IEEE Transactions on Industry Applications*, vol. 44, no. 4, pp. 951–961, 2008.

[19] K. Palka and J. Czyz, "Optimizing downhole fluid production of sucker-rod pumps with variable motor speed," *SPE Production & Operations*, vol. 24, no. 2, pp. 346–352, 2009.

[20] X. Q. Xu, H. B. Zhou, and M. Li, "Research on intelligent frequency conversion control system of pumping unit with auto-adapted function," in *Electronic and Mechanical Engineering and Information Technology (EMEIT), 2011 International Conference on*, vol. 5, pp. 2246–2248, IEEE, 2011.

[21] B. Ordonez, A. Codas, and U. F. Moreno, "Improving the operational conditions for the sucker-rod pumping system," in *Control Applications,(CCA) & Intelligent Control,(ISIC), 2009 IEEE*, pp. 1259–1264, IEEE, 2009.

[22] J. M. Lu, J. P. He, C. X. Mao, W. W. Wu, D. Wang, and W. J. Lee, "Design and implementation of a dual pwm frequency converter used in beam pumping unit for energy saving," *IEEE Transactions on Industry Applications*, vol. 50, no. 5, pp. 2948–2956, 2014.

[23] S. M. Dong, W. C. Li, X. F. Zhao, and R. Zhao, "Frequency conversion beam pumping system dynamic simulation and real time frequency optimization," *China Mechanical Engineering*, vol. 27, no. 12, pp. 1585–1590, 2016.

[24] A. Kusko and D. Galler, "Control means for minimization of losses in ac and dc motor drives," *IEEE Transactions on Industry Applications*, vol. IA-19, pp. 561–570, July 1983.

[25] Z. Y. Wang and J. H. Wang, "Review on implementation and assessment of conservation voltage reduction," *IEEE Transactions on Power Systems*, vol. 29, no. 3, pp. 1306–1315, 2014.

[26] G. O. Garcia, J. C. M. Luís, R. M. Stephan, and E. H. Watanabe, "An efficient controller for an adjustable speed induction motor drive," *IEEE Transactions on Industrial Electronics*, vol. 41, no. 5, pp. 533–539, 1994.

[27] F. Fernandez-Bernal, A. Garcia-Cerrada, and R. Faure, "Model-based loss minimization for dc and ac vector-controlled motors including core saturation," *IEEE Transactions on industry Applications*, vol. 36, no. 3, pp. 755–763, 2000.

[28] R. Saidur, "A review on electrical motors energy use and energy savings," *Renewable and Sustainable Energy Reviews*, vol. 14, no. 3, pp. 877–898, 2010.

[29] A. M. Bazzi and P. T. Krein, "Review of methods for real-time loss minimization in induction machines," *IEEE Transactions on Industry Applications*, vol. 46, no. 6, pp. 2319–2328, 2010.

[30] Y. Zhang, "Induction motor with adjustable windings for high efficiency drive in light load operation," *Journal of Electrical Engineering and Technology*, vol. 9, no. 2, pp. 508–513, 2014.

[31] I. N. Shardakov and I. N. Wasserman, "Numerical modelling of longitudinal vibrations of a sucker rod string," *Journal of Sound and Vibration*, vol. 329, no. 3, pp. 317–327, 2010.

[32] W. Luo, B. Wang, H. S. Zhao, and Y. L. Luo, "Modeling and simulation of non-linear dynamic process of the induction motor system with fluctuating potential loads," *Science China Technological Sciences*, vol. 57, no. 9, pp. 1729–1737, 2014.

[33] S. D. Wee, M. H. Shin, and D. S. Hyun, "Stator-flux-oriented control of induction motor considering iron loss," *IEEE Transactions on Industrial Electronics*, vol. 48, no. 3, pp. 602–608, 2001.

[34] S. G. Gibbs, "Predicting the behavior of sucker-rod pumping systems," *Journal of Petroleum Technology*, vol. 15, no. 7, pp. 769–778, 1963.

[35] M. M. Xing, "Response analysis of longitudinal vibration of sucker rod string considering rod buckling," *Advances in Engineering Software*, vol. 99, pp. 49–58, 2016.

[36] B. Hansen, B. Tolbert, C. Vernon, and J. D. Hedengren, "Model predictive automatic control of sucker rod pump system with simulation case study," *Computers & Chemical Engineering*, vol. 121, pp. 265 – 284, 2019.

[37] Z. S. Chen, L. W. White, and H. M. Zhang, "Predicting sucker-rod pumping systems with fourier series," *SPE Production & Operations*, vol. 33, no. 4, pp. 928–940, 2018.

[38] B. Y. Zheng, X. W. Gao, and X. Y. Li, "Fault detection for sucker rod pump based on motor power," *Control Engineering Practice*, vol. 86, pp. 37–47, 2019.

[39] B. S. Chen, *Electric drive automatic control system*. Beijing, China: Machine Industry Press, 2003.

[40] C. B. Regaya, F. Farhani, A. Zaafouri, and A. Chaari, "A novel adaptive control method for induction motor based on backstepping approach using dspace ds 1104 control board," *Mechanical Systems and Signal Processing*, vol. 100, pp. 466 – 481, 2018.

[41] N. X. Cui, Z. C. Hui, and F. T. Sun, "Study on efficiency optimization and high response control of induction motor," *Proceedings of the Chinese Society of Electrical Engineering*, vol. 25, no. 11, p. 118, 2005.

[42] P. C. Krause, O. Wasynczuk, S. D. Sudhoff, and S. Pekarek, *Analysis of electric machinery and drive systems*, vol. 2. Wiley Online Library, 2002.